

CENTRO DE INVESTIGACIÓN EN
MATEMÁTICAS A. C.

Segmentation of neonatal brain magnetic resonance images

Thesis submitted in fulfilment of the
requirements for the degree of
Master of Science
in Computation and Industrial Mathematics

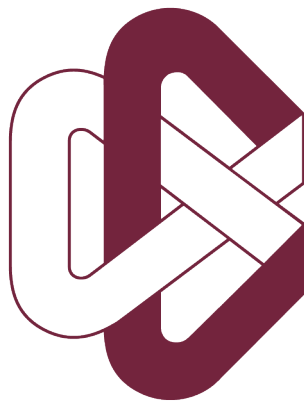
Author:

Ulises Rodríguez Domínguez

Supervisor:

Dr. Oscar Susano Dalmau Cedeño

August, 2016



CIMAT

Certified by:

Dr. Oscar Susano Dalmau Cedeño
Thesis supervisor

Abstract

The segmentation of brain Magnetic Resonance Imaging (MRI) images is known to be a useful computational tool to aid in the medical diagnosis of brain diseases and more generally of diseases related to the central nervous system. This type of segmentation is also an important tool for studying the early infant brain development. Despite the fact that there are many accurate techniques for segmenting the adult brain, those techniques usually do not have the same effectiveness in the infant brain. Furthermore, most of the available segmentation frameworks for brain MRI images usually consist of various pieces of software that are not integrated into a single application. It is therefore the purpose of this work to provide an integrated segmentation framework that is also able to obtain accurate results for the automatic classification of tissues in the infant brain. In particular, the focus of this work is to segment the intracranial cavity (IC) into cortical grey matter (CGM), subcortical grey matter (SGM) and unmyelinated white matter (UWM) tissues of the neonatal infant brain and also into the cerebrospinal fluid (CSF). The proposed segmentation framework is an atlas based one. The framework takes advantage of a particular technique for segmenting each grey matter (GM) tissue, yielding an enhancing stage that was separated into appropriate modules. The latter was considered because, among other issues, in the infant brain the problem of different brain tissues having the same signal intensity is more difficult to solve than in the adult brain. First, an alignment between prior atlas information and the subject to segment takes place, and then both the CGM and SGM together with their corresponding interface with the UWM and CSF are enhanced.

Acknowledgements

I would like to express my gratitude to my supervisor Dr. Oscar Dalmau for giving me the freedom to explore different ideas for this thesis work, for the valuable and enthusiastic discussions we had during the months that this project lasted and for his genuine support.

Thanks to my professors from CIMAT for the transmission of their knowledge and for being an inspiration to work hard. Thanks to the personnel that works at CIMAT for making these two years more comfortable and for their dedication to help the students. Thanks also to my graduate school classmates for the supportive reunions we had once in a while.

To the thesis examining committee: Dr. Jorge Bosch-Bayard, Dr. Luis Concha Loyola and Dr. Mariano Rivera Meraz. Thanks for the valuable comments and suggestions that helped to improve the quality of this thesis work. Also, I would like to thank Dr. Omar Ocegueda González, whose collaboration helped to overcome difficulties encountered during this work.

To my family: Esther, Mauricio, Raquel, Maureen, Almendra and Isabella, who I deeply thank for the supportive environment they have always provided to me. Specially I thank my mother Esther for the encouragement provided to continue on this path.

Finally I would like to thank the CONACyT (National Council of Science and Technology) for the economic support provided in order to accomplish my master degree.

Contents

I	Introduction	7
I.1	Motivation	7
I.2	Problem and challenges	8
I.3	Contributions of the thesis	9
II	Background	11
II.1	Brain MRI segmentation overview	11
II.1.1	Supervised classification techniques	11
II.1.2	Unsupervised classification techniques	12
II.2	Infant brain segmentation	12
III	Overview of the framework and preprocessing	15
III.1	Preprocessing	16
IV	Segmentation	24
IV.1	GM zone enhancing	26
IV.1.1	CGM enhancing	26
IV.1.2	SGM enhancing	33
V	Experiments and discussion of the results	36
V.1	Preprocessing - Intracranial Cavity Extraction	37
V.2	Preprocessing - Registration	37
V.3	Segmentation - CGM enhancing	38
V.4	Segmentation - SGM enhancing	43
V.5	NeobrainS12 challenge results	48
VI	Conclusions and future work	52
VI.1	Future work	52
	References	54

List of Abbreviations

BGT	Basal Ganglia and Thalami
CC	Connected Component
CCs	Connected Components
CGM	Cortical Grey Matter
CSF	Cerebrospinal Fluid
EM	Expectation-Maximization
FA	Fractional Anisotropy
GM	Grey Matter
IC	Intracranial Cavity
ICE	Intracranial Cavity Extraction
MR	Magnetic Resonance
MRF	Markov Random Field
MRI	Magnetic Resonance Imaging
SGM	Subcortical Grey Matter
UWM	Unmyelinated White Matter
WM	White Matter

Chapter I

Introduction

I.1 Motivation

During the first year of life, accurate tissue segmentation of MRI images of the infant brain is of great importance in studying and measuring the normal and abnormal early brain development (L. Wang et al., 2014). Population studies are needed in order to measure different brain tissues and regions of interest in healthy infant subjects and be able to establish a baseline of measures that can help to indentify a healthy infant brain. Measures obtained from population studies of the different tissues of the infant brain can also be valuable for more basic research in areas such as developmental cognitive neuroscience and other related neuroscience areas. Regarding abnormal early brain development, quantitative studies in preterm born neonates using MRI images have identified disturbances in some regions of both GM and white matter (WM) tissues compared to neonates born at term (Makropoulos, 2014). Furthermore, when a non-healthy neonate brain is identified, temporal studies of that subject during the infant period, which include segmentation of its brain tissues in MRI images, are desirable. The latter in order to aid in the medical decisions which aim to improve the health of the infant subject.

Manual segmentation of neonatal brain MRI images carried out by appropriate experts is possible. However, manual segmentation is a very time consuming process that makes both temporal and population studies unfeasible to accomplish within a reasonable period of time in which they are usually needed. In this regard (Makropoulos, 2014) mentions that besides being a very time consuming process, manual segmentation of MRI images is subject to inter- and intra-observer variability. Since such variability depends on human intervention, and it is not desired when segmenting neonatal brain MRI images, especially for population studies, an automatic way of doing it is more desirable. Currently there are several methods available to segment MRI images of the adult brain, however they either do not have the same effectiveness when attempting to segment neonatal brain MRI images or they have to be adapted to be able to work well in the neonatal case.

Finally, both in the neonatal and in the adult case, the segmentation frameworks available usually consist of various separated pieces of software that have to be applied to the subject images stage by stage. The goal of having an automatic segmentation framework available as a software is for it to be available to

any non-technical user. Nonetheless, a non-integrated segmentation framework software makes the segmentation process unnecessarily more difficult for the final user. Because of all of the previous reasons, an accurate automatic and integrated segmentation framework for MRI images of the neonatal brain is highly desirable and is the purpose of this thesis work. As a common reference for evaluation purposes of the segmentation framework presented here, a recent segmentation challenge was used, namely NeoBrainS12, which has been open since 2012 and presents challenges specific for segmenting neonate brain MRI images.

I.2 Problem and challenges

The automatic segmentation of an image consists of generating a new image, based on the original one, by applying a mask over the object of interest in the original image in an automatic way. The previous is equivalent to labeling the region of interest of the image according to the object class to which it belongs. This labeling can be applied in a more general way to many classes of interest within the image. In the specific context of MRI images of the brain the classes of interest are typically those corresponding to GM, WM and CSF tissues; however, there are also other possible classifications. Even though segmentation in this context has received a lot of effort and resources during the last years there is still not a complete solution to the problem. The latter is true mainly because of the great complexity of the problem, the multiplicity of the experimental situations and because researchers sometimes focus just in a small amount of data (Manjón Herrera, 2006). Some of the most common problems when attempting to segment MRI images of the brain are the following:

- **Partial volume**
This effect is the mixing of different tissue classes in a single voxel and is evident in the tissue boundaries (Makropoulos, 2014). (Manjón Herrera, 2006) mentions that due to the finite resolution of the measuring devices during the acquisition of the MRI images this is an inevitable effect.
- **Inhomogeneity**
This artifact caused by non-uniform radio-frequency fields and reception sensitivity as well as electromagnetic interaction with the body of the subject results in non-uniform intensity of a single tissue class over the image space (Makropoulos, 2014).
- **Noise**
This can be caused by electromagnetic noise in the body of the subject and small anomalies in the reception electronics (Makropoulos, 2014).

In addition to the previous problems, automatic segmentation of MRI images of the neonatal brain presents an even more challenging scenario due to the following reasons:

- Reduced contrast between WM and GM
There is a myelination process in some of the nerve fibers in the infant brain and the myelin makes the WM appear darker in the MRI T2 images as the infant brain develops (Roselli, Matute, & Ardila, 2010). (L. Wang et al., 2014) made a distinction between three stages in the infant brain MRI images. The first stage is the infantile stage (less or equal than 5 months) in which the GM shows a higher intensity than the WM in T1 images. Then, in the isointense stage (from 6 to 12 months) is where it becomes more difficult to differentiate between GM and WM intensity in both T1 and T2 images because of the myelination process of the WM. Finally in the early adult-like stage (greater than 12 months) the GM intensity is much lower than that of the WM in T1 images. An intensity histogram of a MRI T2 neonate image is shown in Figure I.1.
- Greater occurrence of motion artifacts
Compared to the case of the adult brain there is an increase of this type of artifacts that result in mis-aligned image slices and ghosting effects (Makropoulos, 2014).
- Greater variation of shape and appearance
Due to dendritic and myelination processes of some nerve fibers the brain presents a rapid development after birth (Roselli et al., 2010).
- Thin cortical gray matter
The sheet-like structure of the CGM is more thin in the neonatal brain than in the adult brain. The thin CGM, the partial volume effect and the great variation of the shape of the CGM, make it very difficult to delineate in an automatic way the gray matter at the cortical regions.

I.3 Contributions of the thesis

The aim of this thesis is to provide an automatic and integrated segmentation framework for MRI images of the neonatal brain that is able to obtain accurate results for separating the UWM, CGM and SGM tissues and the CSF. The proposed segmentation framework is atlas based and it uses different techniques in the GM tissues by separating the process into modules. It makes use of a morphological approach to separate the Intracranial Cavity (IC) from the background. In order to guide the segmentation at different stages and in order to segment the majority of the UWM tissue it makes use of an atlas based approach by considering a priori knowledge of an individual neonatal brain atlas that allows to introduce spatial consistence. It also considers Hessian information and non-local similarity patches together with local information to obtain the improved segmentation results at both the CGM and SGM zones respectively. Chapter II describes methods and techniques applied to the segmentation of brain MRI images and state-of-the-art methods for the segmentation of infant brain MRI images. Chapter III presents the overview of the segmentation framework and describes the preprocessing steps to apply to an MRI image of the neonatal brain. The preprocessing steps are similar to those applied in a morphological approach in order to help decrease some of the mentioned artifacts

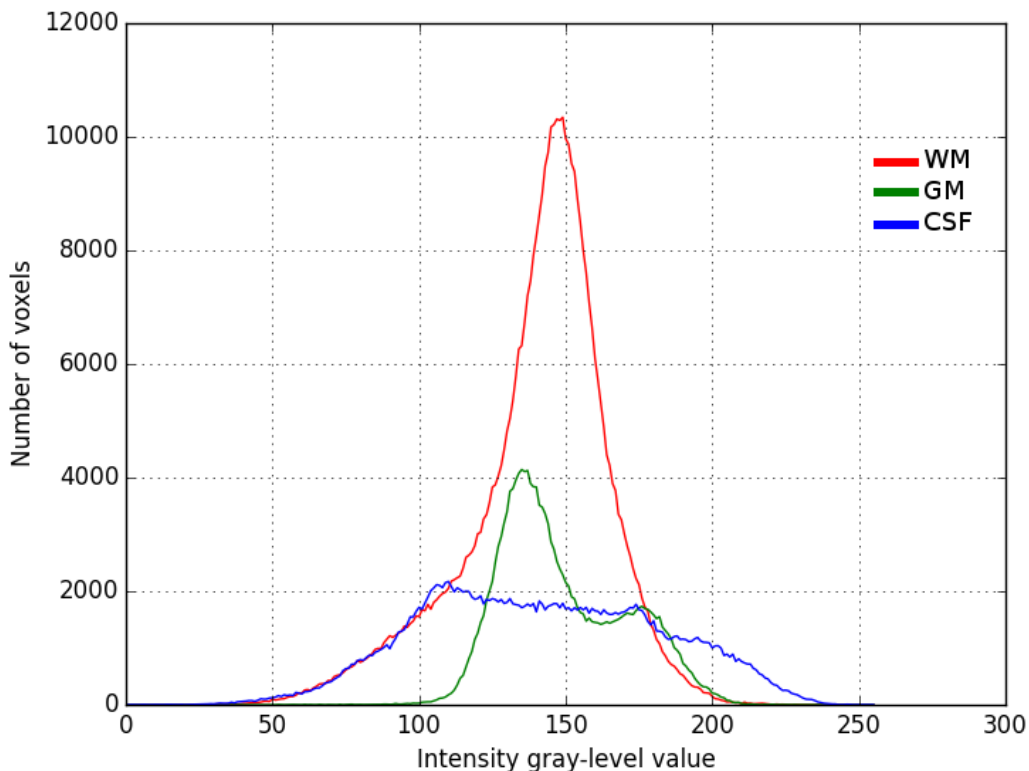


Figure I.1: Intensity histograms of WM, GM and CSF tissues corresponding to the 30 weeks coronal second training volume example of the NeobrainS12 (2012) challenge. The volume is a T2 brain MRI image of a 30 weeks old (corrected age) neonate.

and keep only the Intracranial Cavity (IC). However, different registration steps are also considered during preprocessing. Chapter IV describes the segmentation of neonatal brain tissues stage in this framework. The segmentation stage starts with label information from tissues from an aligned neonatal brain atlas as a starting point and then refines both the CGM and SGM zones. The corresponding interfaces of both GM zones with the UWM and CSF are also refined at the segmentation stage to provide the improved results. Because of the difficulty of having an integrated segmentation tool for MRI images of the brain, this thesis also contributes a segmentation framework software for MRI images of the brain of neonates. The software, written in Python, will be made freely available in the future and includes all of the stages of the proposed framework except for the initial intensity inhomogeneity correction. Data from the (NeoBrainS12, 2012) challenge, available at <http://neobrain12.isi.uu.nl>, was used to develop the segmentation framework here presented. Chapter V describes the experiments made and discusses the obtained results which are compared to state-of-the-art research results obtained so far in the (NeoBrainS12, 2012) challenge. Finally, chapter VI presents the conclusions and future work.

Chapter II

Background

Section II.1 presents a brief overview of the main different types of techniques used for brain MRI segmentation. Then, section II.2 presents methods recently available in the literature for segmenting the infant brain or part of the infant brain.

II.1 Brain MRI segmentation overview

The main types of techniques used for brain MRI segmentation can be classified into the following categories:

II.1.1 Supervised classification techniques

This type of techniques require previously established expert knowledge about how to classify the data of interest. Supervised classification can be further classified as:

- **Non-automatic classification**
In the case of brain MRI segmentation this is done by manual labeling of each voxel of a brain MRI image by medical experts. This modality of supervised classification is extremely time consuming and undesirable for studying the brain of a population of infants because of the inter- and intra-observer variability inherently introduced (Makropoulos, 2014).
- **Semi-automatic classification**
This type of classification incorporates automatic classification only partially to reduce the non-automatic classification work done by the human experts. Human intervention is sometimes carried out in this modality by roughly labeling part of the data of interest with the correct labels to introduce a starting point so that then an automatic computational algorithm can be further applied.
- **Automatic classification**
Given previously labeled examples of the data of interest by human experts in a non-automatic or semi-automatic manner, this type of supervised classification does not require further human intervention to classify new data of interest. Instead a model of the data is learned from the labeled examples and then is used to classify the new data. It is important in this modality to have sufficient

labeled examples (training data) so that the learned model can then classify new data in a general way.

A very common scheme for supervised classification in the segmentation of brain MRI images is the following:

- Atlas-based classification
Atlas based methods take advantage of segmented templates already available that are either taken as "ground truth" or as guidelines to help in the segmentation process. The used templates are usually segmented manually by experts and those intensity templates are typically aligned to the MRI images that need to be segmented by some registration algorithm.

II.1.2 Unsupervised classification techniques

This type of techniques do not require training data and they use a similarity measure to classify the unlabeled data of interest (Makropoulos, 2014). The following are examples of this type of techniques:

- Clustering
This type of segmentation classifies the data of interest into different classes such that data points (voxels in the case of MRI images) in each group share similar properties and dissimilar properties with data points of other groups. Thresholding based on an image intensity value is a special case of clustering.
- Deformable models
These models segment a region of interest in an image by deforming a closed surface based on a physical model (Makropoulos, 2014). They incorporate geometrical information during their segmentation procedure.
- Edge detection
This type of methods delimitate the regions of interest in an image according to edges found over the signal used to segment the image, which may be the original intensity image or some other signal derived from it.
- Morphological operations
Morphology based methods allow the selection of objects of interest in the image by using a combination of morphological operators (Manjón Herrera, 2006). These morphological operators can take place either on binary images or on grayscale images and are composed by or based on dilation and erosion.
- Region growing
Given a seed region of voxels or pixels in an image this technique iteratively adds more neighbouring voxels or pixels based on a similarity criterion with the region.

II.2 Infant brain segmentation

The following automatic methods for segmenting the infant brain are mainly based on either atlas information or in morphological operations and some of them also use clustering, deformable models, edge detection and region growing techniques.

Integration of sparse multi-modality representation and anatomical constraint for iso-intense infant brain MR image segmentation

This atlas-based method by (L. Wang et al., 2014) segments MRI images of the infant brain in the iso-intense stage by taking advantage of three types of image modality: T1, T2 and fractional anisotropy (FA). The justification for using those image modalities is that, according to (L. Wang et al., 2014) in the iso-intense infant stage, that is from 6 to 12 months of age, the intensity distributions of WM and GM are largely overlapped due to the ongoing maturation and myelination processes. This method represents the T1, T2 and FA subject MRI images in a sparse way based on similarity of patches in the subject images with patches in a set of corresponding atlas templates by dictionary learning. It also uses sparse representation to impose an anatomical constraint to improve the segmentation results. A disadvantage of this method is that it requires approximately twenty atlas templates for obtaining good results, each one with its corresponding T1, T2 and FA MRI images and its labeled segmentation image, which can be unfeasible because of the extremely time-consuming manual labelling of infant brain MRI images. Furthermore, using the T1, T2 and FA modalities implies a longer image acquisition time, which is non-trivial in the neonatal population.

Morphology-driven automatic segmentation of MR images of the neonatal brain

This method by (Gui et al., 2012) uses high-level morphology knowledge of the neonatal brain to segment into different tissues without using an anatomical atlas, hence avoiding atlas-related bias. This method obtained good results in the (NeoBrainS12, 2012) challenge. The type of morphological knowledge used includes relative tissue location, connectivity and structure of different parts of the neonatal brain. During its various stages for segmenting the neonatal brain this method uses morphological operations, the marker-based and similarity-based watershed algorithm, region growing and 3D region-based active contour segmentation which is a deformable model type of method.

Automatic registration-based segmentation for neonatal brains using ANTs and Atropos

This method by (Wu & Avants, 2012) uses an atlas intensity template according to the neonate subject age and registers it to the MRI images of the neonate subject in order to have the corresponding atlas tissue priors aligned with the subject space. It obtained reasonable results in the (NeoBrainS12, 2012) challenge. After intensity inhomogeneity correction, this method performs the segmentation of the brain tissues with Atropos, which is based on a multivariate Markov Random Field (MRF) method, restarting the process three times by setting the output probability maps of the previous iteration as input probability maps of the next iteration. The input for the first iteration are the initially registered atlas tissue priors. Since the quality of this method greatly depends on the quality of the chosen atlas template it had suboptimal CSF segmentation due to the fact that their chosen template did not have features outside of the cerebrum.

Automatic MRI segmentation of the developing neonatal brain

This method by (Makropoulos, 2014) is among the methods that achieved the most accurate results in the (NeoBrainS12, 2012) challenge and is based on an Expectation-Maximization (EM) scheme. It propagates spatial priors from an atlas of the neonatal brain corresponding to the age of the subject with a relaxation technique to account for adaptivity to each individual subject and a MRF regularization to account for spacial dependency of neighbouring voxels.

Cortical enhanced tissue segmentation of neonatal brain MR images acquired by a dedicated phased array coil

(Shi et al., 2009) enhanced the CGM zone in MRI images of the neonatal brain by combining a population atlas with a prior of the sheet-like CGM structures, which are detected by means of a Hessian filter. Then, they called that combination a subject-specific atlas and used it to obtain improved segmentation results of the neonatal brain. However, for their improved segmentation results they also used a dedicated phased array neonatal head coil to combine images obtained from eight coil elements during the acquisition stage which may not always be possible to have depending on the resources available for the imaging task.

Chapter III

Overview of the framework and preprocessing

The proposed segmentation framework is summarized in Figure III.1. Before the actual segmentation of the brain tissues of a neonate into CGM, SGM, UWM and CSF, standard preprocessing steps are applied similarly to those applied in (Gui et al., 2012). In order to evaluate the proposed framework on a common reference of data and acquisition parameters, the (NeoBrainS12, 2012) challenge was used. The data was taken from <http://neobrain12.isi.uu.nl>. The (NeoBrainS12, 2012) challenge data was also used during the development phase of the framework. In particular, in this work the set of neonatal brain images corresponding to 30 weeks of corrected age was used, which includes two volumes for training with their corresponding manual segmentations and five volumes for testing. The selected set corresponds to MRI images from pre-term born neonates acquired on a Philips 3T system at the University Medical Center Utrecht, The Netherlands, see (Işgum et al., 2015). The acquisition protocol for the coronal 3DT1-weighted images (referred in this work as T1 images) is: TR=9.4 ms; TE=4.6 ms; scan time=4.44 min, FOV=130x100; reconstruction matrix=384x384; consecutive sections with thickness=2.0 mm; number of sections=50, in-plane resolution 0.34 mm x 0.34 mm (NeoBrainS12, 2012). For the case of the coronal T2-weighted images (referred in this work as T2 images), the acquisition protocol is: TR=10085 ms; TE=120 ms; scan time=6.23 min; FOV=130x100; reconstruction matrix=384x384; consecutive sections with thickness=2.0 mm; number of sections=50, in-plane resolution 0.34 mm x 0.34 mm (NeoBrainS12, 2012). All of the volumes include the subject's MRI T1 and T2 images. The input to the framework are the T1 and T2 MRI images of the infant subject and an individual brain atlas which includes a T1 and T2 MRI image with its corresponding segmentation indicated by an image of class labels. The brain atlas is selected so that it corresponds to a neonate of the same weeks of corrected age as the subject to segment. The parameters of the framework were first tuned by using one of the training volumes as the input subject and the remaining training volume as the infant brain atlas and then the same was carried out but switching the role of each training volume. The general idea of the framework is to first align the available atlas information to the subject space to have an initial state with anatomical consistence for the different brain tissues of interest and then refine the GM segmentation at both the CGM and SGM zones. The framework, written in Python and which integrates all of the steps described in this work with the exception of the initial bias field

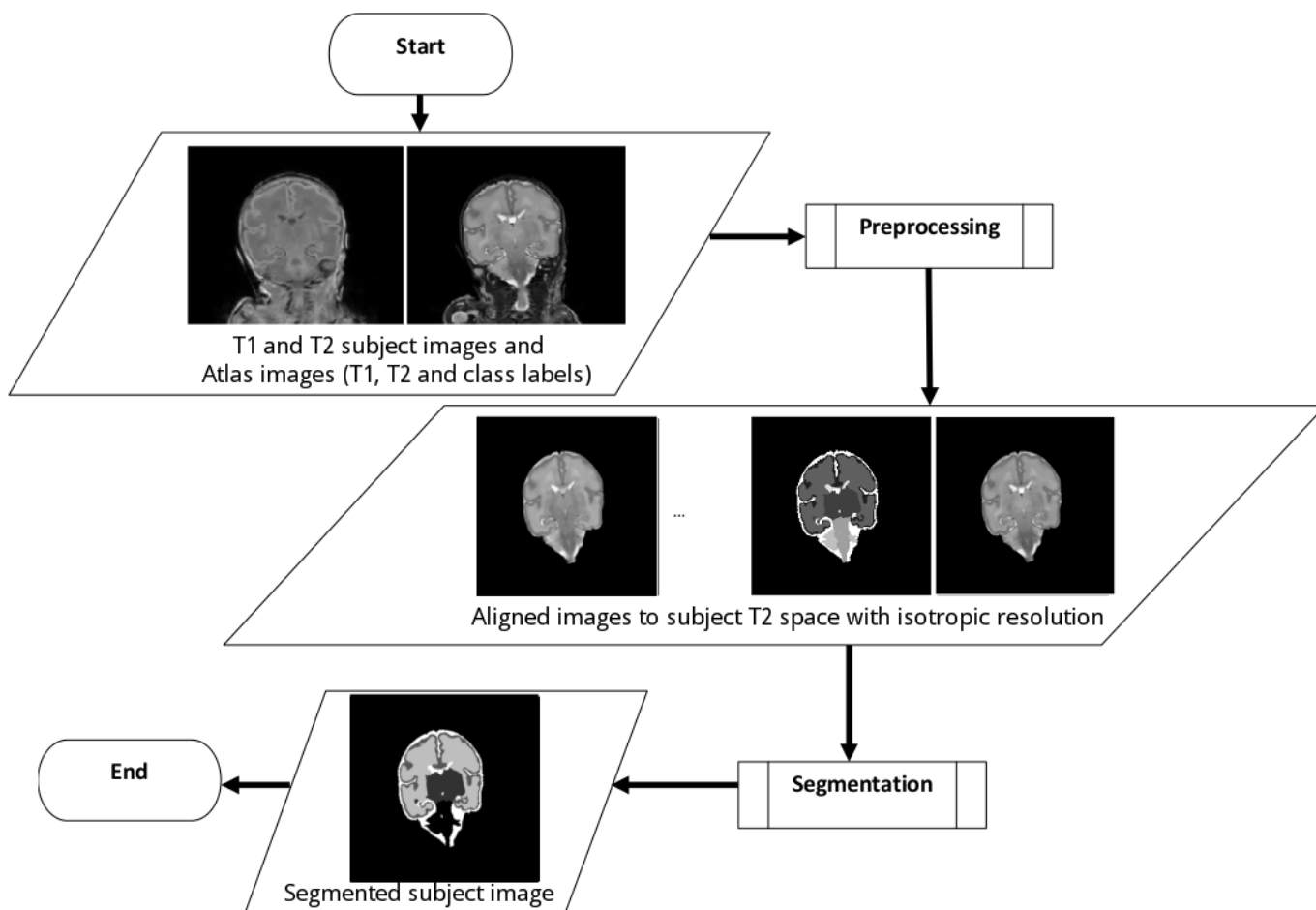


Figure III.1: Flowchart with the overview of the segmentation framework. Given the subject’s T1 and T2 MRI images and the atlas images (T1, T2 and class labels), preprocessing steps are first applied on the images. The latter results in the alignment of all the images to the subject’s T2 image space and in regions that are neither brain nor CSF removed. Then, after the segmentation stage is carried out, the segmented subject image is obtained.

correction, will be made freely available in the future.

III.1 Preprocessing

The preprocessing steps of the segmentation pipeline are summarized in Figure III.6 and are similar to those applied in (Gui et al., 2012) but considering also registration steps. The following is the description of each step.

Bias field correction: First intensity inhomogeneity correction is applied to both subject images using the N4 bias field correction algorithm implemented in the 3DSlicer software version 3.6.3 based on (Tustison et al., 2010).

Affine registration 1: Affine registration of the subject’s T1 image to the subject’s T2 image is then applied followed by an affine registration of the atlas T2 image (masked with the labels image to include only the IC) to the subject’s T2 image. The atlas affine registration transform obtained is then applied to also transform the atlas brain labels image to the subject T2 image space. The latter is carried out with the purpose of having an initial rough IC mask that can aid during the Intracranial Cavity Extraction (ICE). (L. Wang et al., 2014) noted that when different brain MRI image modalities come from the same subject, they share the same brain anatomy and therefore can be accurately aligned with only rigid registration. However, in this work no assumption is made because the CSF is also of interest, and movements in the infant subject’s head could produce slight changes between the subject MRI images in the CSF regions. The latter is the reason that affine registration between the subject’s T1 and T2 image was selected. The T2 image of the subject was chosen as the common space for aligning the rest of the images because in the case of the training examples from the (NeoBrainS12, 2012) challenge it is already aligned with the subject’s manual segmentation image and because of better contrast in the T2 images. Furthermore, chapter IV in the Preprocessing - Registration subsection presents experiments made that demonstrate better segmentation results when registration is carried out exclusively between images in the T2 modality. Figure III.2 shows coronal slices of the masked atlas T2 image corresponding to 30 weeks of corrected age affinely aligned with the corresponding training T2 image volumes. The affine registrations in this step and in the following steps are carried out using Dipy’s registration module (Garyfallidis et al., 2014) based on ANTS (B. Avants, Tustison, & Song, 2009).

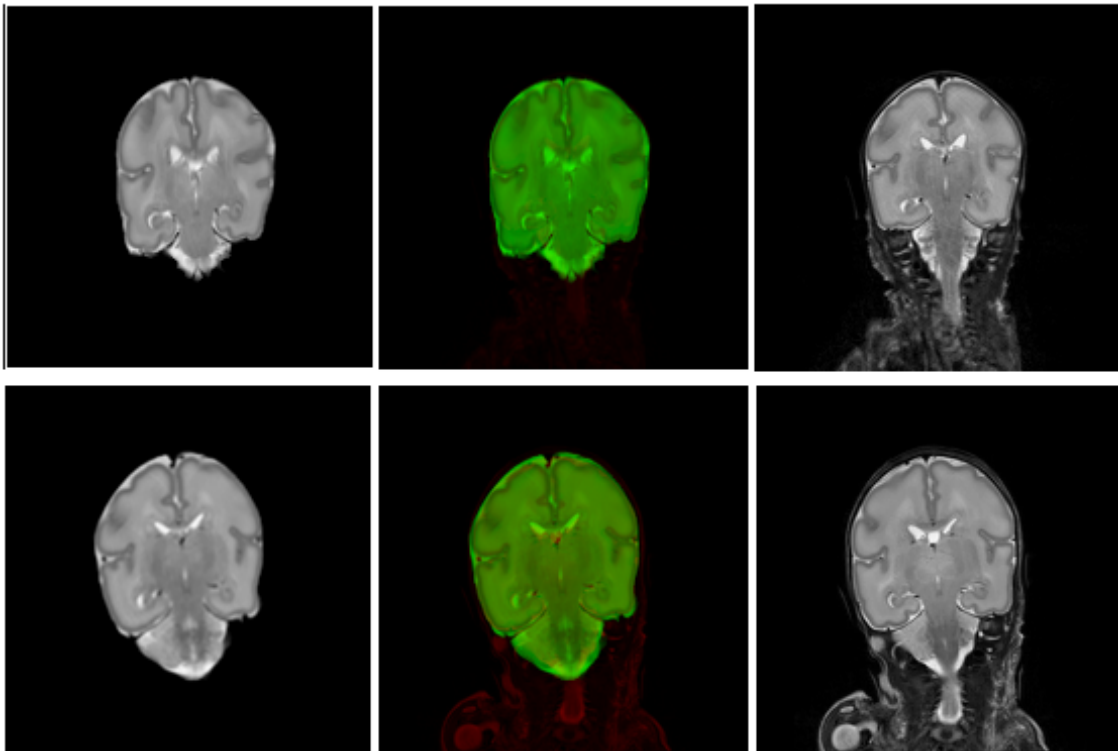


Figure III.2: Coronal slices showing the affinity aligned atlas T2 images (masked previously with the labels image to include only the IC) with the training T2 image volumes. All images correspond to subjects at 30 weeks of corrected age. The top row corresponds to the first training volume while the bottom row corresponds to the second training volume. *Left column:* atlas images. *Right column:* subject training images. *Middle column:* overlay of both images by combining a red color channel for the right column images with a green color channel for the left column images.

Isotropic scaling: The previous step is followed by isotropic voxel scaling of the subject images and of the affinity registered atlas labels image by using Dipy (Garyfallidis et al., 2014). This step helps to improve the results of the morphological operations used for performing the ICE. Furthermore, in chapter IV in the Preprocessing - Intracranial Cavity Extraction subsection it is experimentally demonstrated that isotropic voxel scaling improves the ICE over not using isotropic voxel scaling.

ICE: As the next preprocessing step, ICE is performed in a similar way to (Gui et al., 2012) because of the simplicity of implementation, good results obtained and in order to avoid further dependence on external software for the segmentation framework. For this step first a brain mask is constructed by setting as foreground the regions of the affinity aligned atlas labels image that are not zero and as background the regions that are zero. Then that atlas brain mask is dilated with a big enough structuring element so that it can incorporate with confidence the true brain regions and the CSF of interest of the subject image. A sphere of 19 voxel units of diameter is chosen as a structuring element for the dilation. The resulting brain mask is applied on the T2 subject image resulting in the image S_{T2-M} and then the following operations (with most of the notation taken as in (Gui et al., 2012)) are applied in

order to obtain the ICE image S_{T2-ICE} :

$$S_{T2-ICE}(r) = \delta_{B_3} \left[Watershed \left[\sum_{i=0}^4 \delta_{B_{2i+1}} [grad [\gamma_{B_9} [S_{T2-M}]]] \right] \right] (r) \quad \forall r \in I \quad (1)$$

where $r = (x, y, z)$ is a voxel index, I is the subject image domain and letting $f : I \subset Z^3 \mapsto N$, the functions used are defined as follows

- $\delta_B[f]$: the morphological dilation of f by the structuring element B ;
- $\varepsilon_B[f]$: the morphological erosion of f by the structuring element B ;
- $\gamma_B[f]$: the morphological opening of f by the structuring element B
that is $\gamma_B[f] = \delta_B[\varepsilon_B[f]]$;
- $grad[f]$: the thick morphological gradient of f , that is
 $grad[f] = \delta_{B_{3c}}[f] - \varepsilon_{B_{3c}}[f]$;
- $Watershed[f]$: marker-based watershed segmentation of f , carried out by
setting as an internal marker the voxels that indicate SGM
in the atlas labels image and as an external marker the voxels
that do not belong to the dilated and binarized atlas labels
image;
- B_n : the 3D spherical structuring element of n voxel units of
diameter;
- B_{3c} : the 3D symmetrical cross structuring element of 3 voxel units
of diameter.

Equation (1) can be described in words as follows: first a morphological opening is applied on the masked T2 subject image with a sphere as structuring element with 9 voxel units of diameter. Then the morphological gradient of the opened image is computed using a 3D symmetrical cross structuring element of 3 voxel units of diameter. The segmentation function is then computed by summing 5 consecutive scale dilations of the obtained morphological gradient. The dilations are computed with a sphere as structuring element starting from a sphere with 1 voxel of diameter, which produces the same original morphological gradient, up to a sphere with 9 voxels of diameter, increasing each time the diameter by 2 voxel units. The marker based watershed segmentation algorithm is then applied on the sum of dilations image by setting as an internal marker the voxels that indicate SGM in the atlas labels image and as an external marker the voxels that do not belong to the dilated and binarized atlas labels image. The result of the latter is the segmentation into an IC region and a background region. Finally a morphological dilation with a sphere structuring element that produces a minimal expansion, that is a sphere of 3 voxel units of diameter, is performed in order to recover to some degree true CSF regions that were misclassified at the interface with the background voxels. The parameter values used were set as recommended in (Gui et al., 2012), except for the last structuring element used in the final dilation, since such dilation is not used in (Gui et al., 2012), and the structuring element used for dilating the initial brain

mask, given that registration is not used in (Gui et al., 2012). The study of both of the latter parameters is recommended for future work. Figure III.3 shows coronal slices of the morphological gradients, the sums of morphological gradient dilations, the markers for the watershed segmentation and the result of the ICE on T2 images corresponding to the training volumes of subjects at 30 weeks of corrected age. The ICE mask is then applied on both the subject’s T1 and T2 images. The bounding box of the IC is also computed to reduce computations over all the aligned images for the next steps in the segmentation framework.

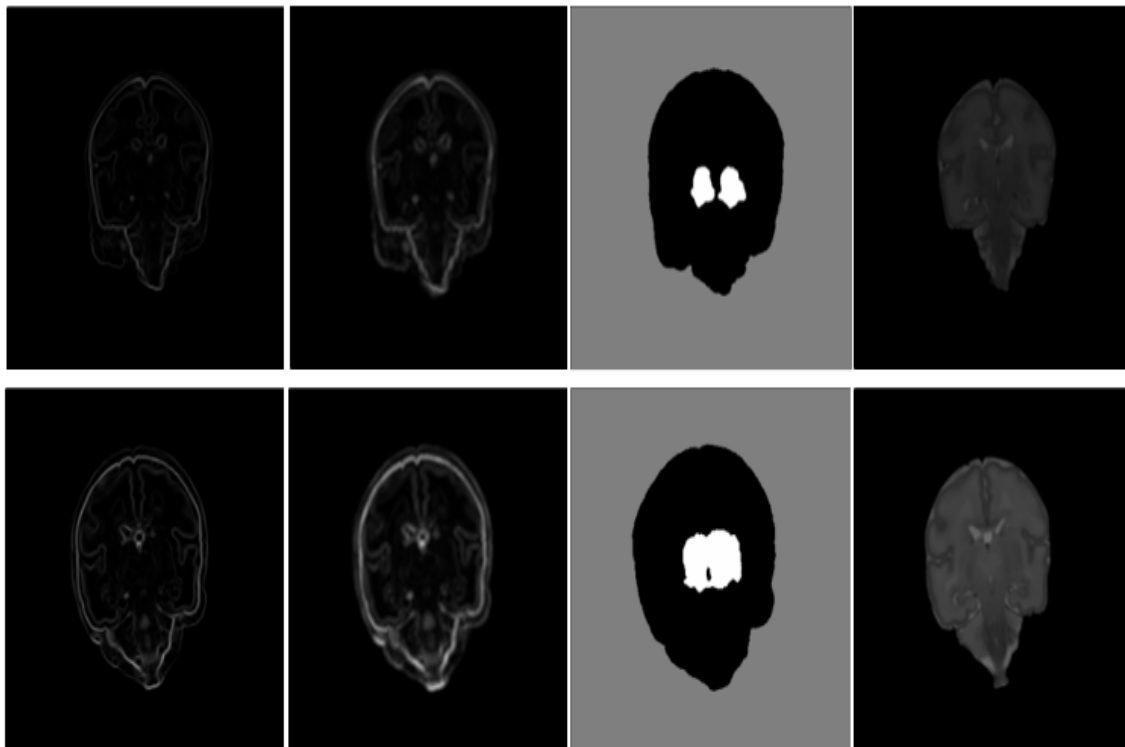


Figure III.3: Coronal slices showing the ICE process corresponding to the training T2 image volumes. All images correspond to subjects at 30 weeks of corrected age. The top row corresponds to the first training volume while the bottom row corresponds to the second training volume. The columns from left to right correspond to the following stages. *First column*: morphological gradient images. *Second column*: sums of morphological gradient dilations (segmentation functions). *Third column*: internal markers (in white) and external markers (in gray) for the watershed segmentation. *Fourth column*: subject T2 training images after ICE.

Affine registration 2: Affine registration of the atlas T2 image (masked with the labels image to include only the IC) to the subject’s T2 image after ICE is performed. The atlas affine registration transform obtained is taken as a starting point for the next diffeomorphic registration step. Figure III.4 shows coronal slices of the masked atlas T2 image corresponding to 30 weeks of corrected age affinely aligned with the corresponding training T2 image volumes after ICE.

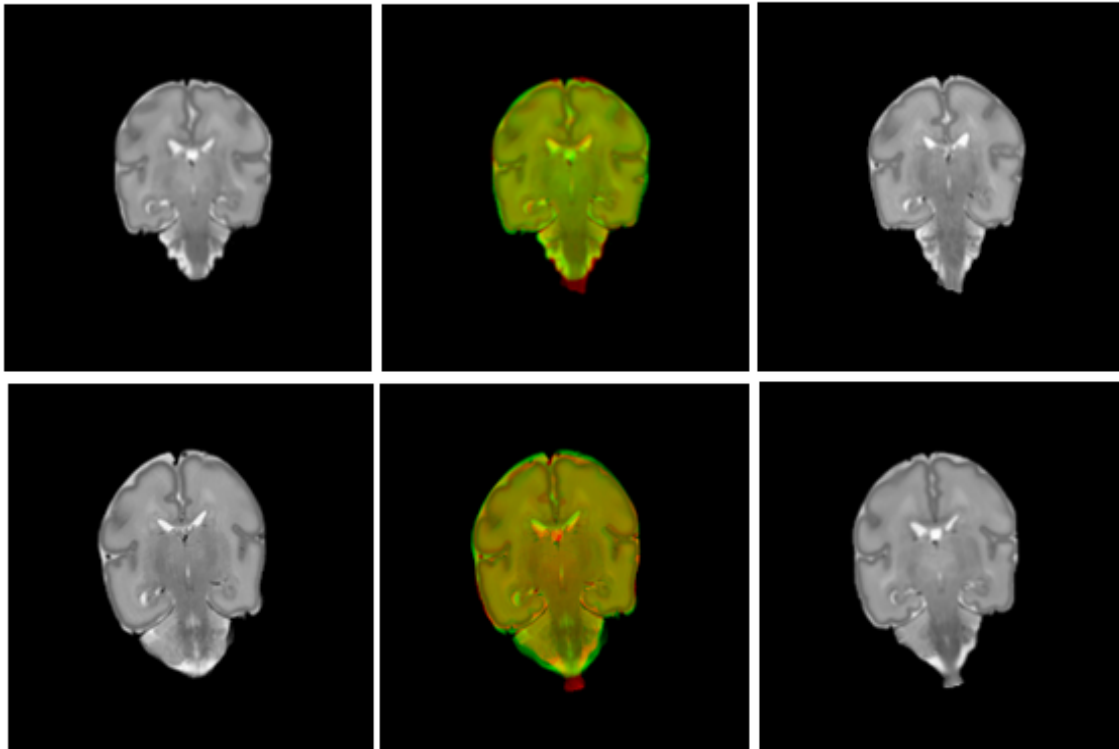


Figure III.4: Coronal slices showing the affinely aligned atlas T2 images (masked previously with the labels image to include only the IC) with the training T2 image volumes after ICE. All images correspond to subjects at 30 weeks of corrected age. The top row corresponds to the first training volume while the bottom row corresponds to the second training volume. *Left column:* atlas images. *Right column:* subject training images. *Middle column:* overlay of both images by combining a red color channel for the right column images with a green color channel for the left column images.

Diffeomorphic registration: Starting with the affine registration transform obtained in the previous registration step, diffeomorphic registration between the atlas T2 image (masked with the labels image to include only the IC) to the subject’s T2 image after ICE is performed. The atlas diffeomorphic registration transform obtained is then applied to the atlas labels image and the atlas T1 image (masked also with the labels image to include only the IC). Figure III.5 shows coronal slices with the diffeomorphic registration results between the masked atlas T2 image corresponding to 30 weeks of corrected age and the corresponding training T2 image volumes after ICE. The diffeomorphic registration is done with the Symmetric Normalization algorithm proposed by (B. B. Avants, Epstein, Grossman, & Gee, 2008; B. B. Avants et al., 2011). For this, the fast implementation proposed by (Ocegueda, Dalmau, Garyfallidis, Descoteaux, & Rivera, 2016) which is also implemented in Dipy (Garyfallidis et al., 2014) and uses a very efficient implementation of cross-correlation is used in this work. After the diffeomorphic registration, the ICE in the subject images is further refined by setting as background (with zero values) the regions that are background in the atlas diffeomorphic registration. The further ICE refinement is applied because those brain regions that could not be matched

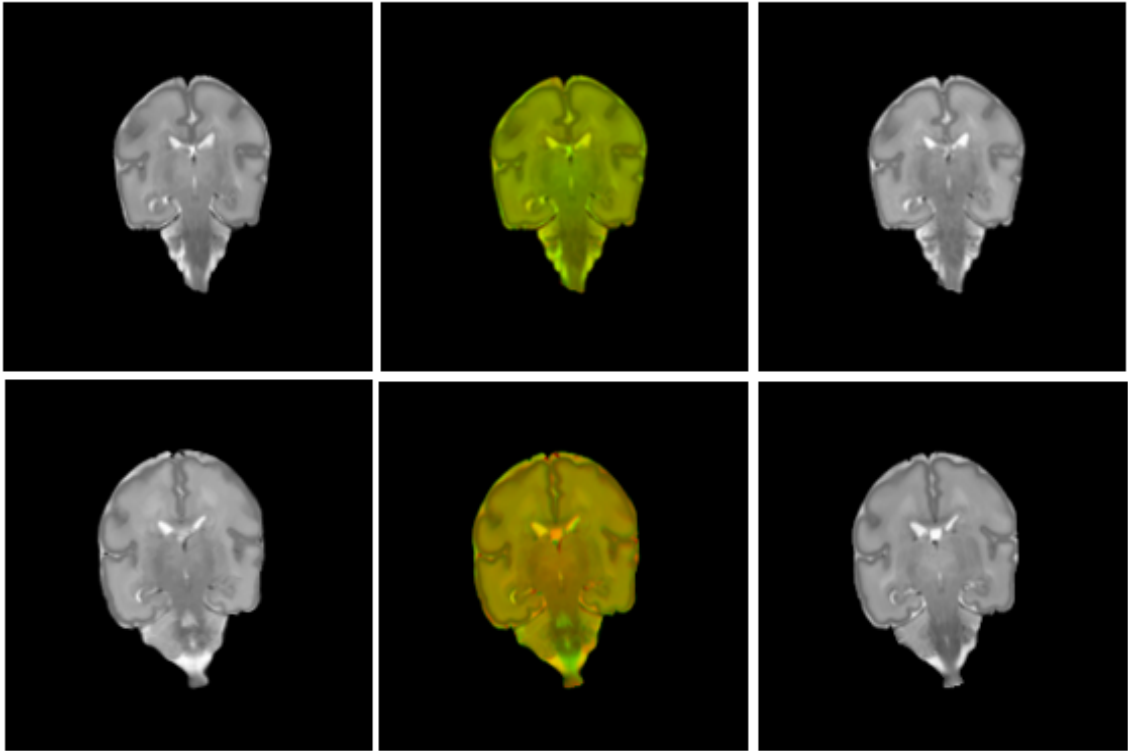


Figure III.5: Coronal slices showing the diffeomorphic registration results of the atlas T2 images (masked previously with the labels image to include only the IC) with the training T2 image volumes after ICE. All images correspond to subjects at 30 weeks of corrected age. The top row corresponds to the first training volume while the bottom row corresponds to the second training volume. *Left column:* atlas images. *Right column:* subject training images. *Middle column:* overlay of both images by combining a red color channel for the right column images with a green color channel for the left column images.

by the diffeomorphic registration algorithm even after the ICE are less likely to be true brain regions consistent with the known brain regions of the atlas.

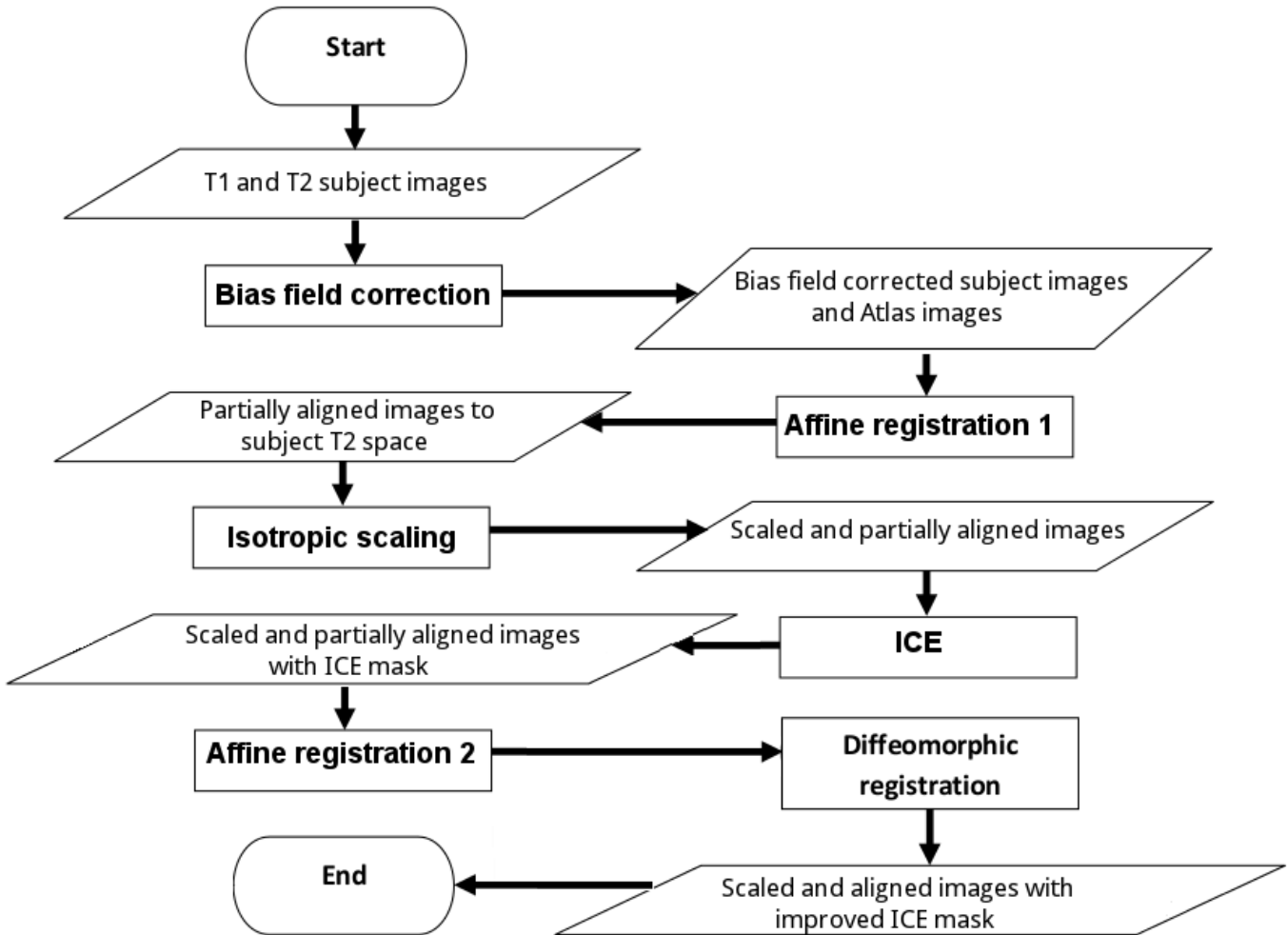


Figure III.6: Flowchart with the preprocessing steps. The bias field correction step is first applied on the subject's T1 and T2 images to correct inhomogeneities in their intensity signal. Then, the subject T1 image is affinely aligned to the subject T2 image, and a masked atlas T2 image (containing only the IC) of the corresponding age is also affinely aligned with the subject T2 image. The latter yields a rough alignment with the atlas that is used to aid the ICE step. After the previous, isotropic scaling is applied to help improve the result of the morphological operations used at later steps. Next, ICE is applied in order to remove the regions that are neither brain nor CSF, which is taken advantage of by registering once again the masked atlas T2 image (containing only the IC) to the subject T2 image after ICE with an affine registration followed by a diffeomorphic registration. The previous results in a better alignment of the atlas images to the subject T2 image space. Finally the ICE is further improved by masking the subject IC images with the resulting atlas IC images after diffeomorphic registration.

Chapter IV

Segmentation

Given the various challenges involved in this particular segmentation task, which were presented in chapter I, the proposed segmentation stage in this thesis work starts with a priori information from the aligned atlas labels image and then refines each GM zone in a modular way. The previous in order to have both a more clear and maintainable framework and in order to easily apply different strategies depending on the particular challenges each GM tissue presents. The proposed segmentation stage consists of only one main stage depicted in Figure IV.1. Since a reasonably good initial segmentation is already available at the beginning due to the previous diffeomorphic registration that takes advantage of the ICE, no further initial refinement is applied. Because of the previous, both the CGM and SGM zones are then improved yielding also complementary improvement in the UWM and CSF tissues at the boundary zones with either GM tissue by using a combination of a Hessian filter with a box filter and post-processing operations for the CGM and a local neighbourhood together with non-local similarity patches for the SGM.

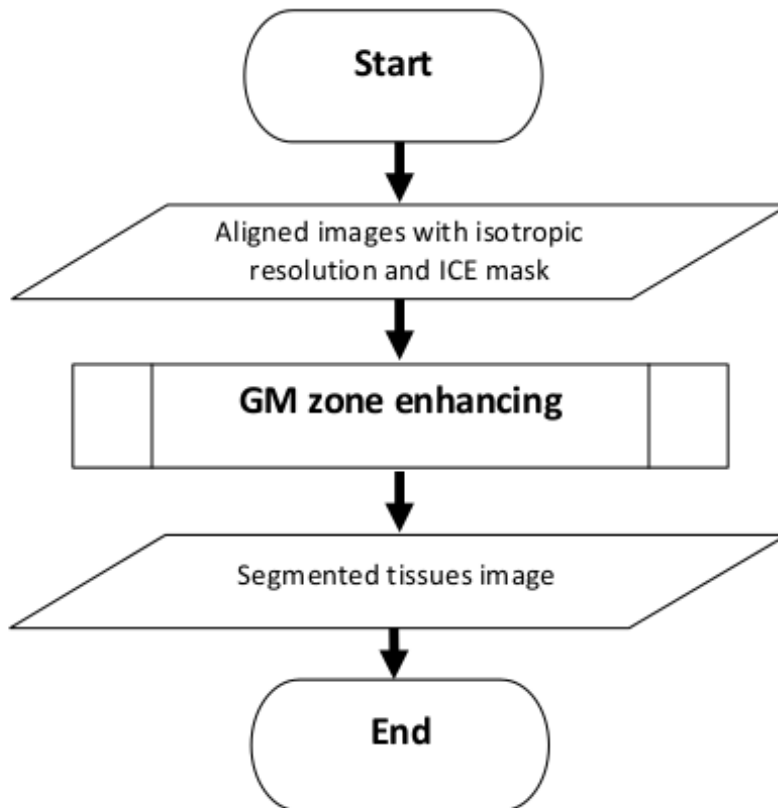


Figure IV.1: Flowchart of the segmentation stage. This stage assumes that all of the images have been preprocessed, with the corresponding masked atlas images already in the subject’s T2 image space. The segmentation consists of one main step: starting from the aligned atlas tissue labels, the GM tissues are further enhanced at both the CGM and SGM zones, producing also complementary improvement at their interface with other brain tissues.

The segmentation stage is presented in more detail in Algorithm 1 and then further details are presented in the section IV.1. The variables and user-defined parameters used in Algorithm 1 are defined as follows:

- S_{T_2} : Subject T2 preprocessed MRI image.
- S_{T_1} : Registered subject T1 preprocessed MRI image.
- A_{T_2} : Registered atlas T2 preprocessed MRI image.
- A_{T_1} : Registered atlas T1 preprocessed MRI image.
- $A_{\mathcal{K}}$: Registered atlas labels image. $\mathcal{K} = \{k_1, k_2, k_3, k_4, k_5\}$ is the set of labels where k_1, k_2, k_3, k_4 and k_5 correspond to the background, CSF, UWM, CGM and SGM classes respectively.
- B : Bounding box coordinates of the IC mask.
- v_s : Physical voxel spacing in millimeters that each isotropic voxel represents.
- P_1 : First set of two parameters used during the CGM enhancing stage.
- P_2 : Second set of four parameters used during the SGM enhancing stage.
- S_M : Segmentation map.

Algorithm 1 Segmentation of the S_{T2} MRI subject image.

Require: $S_{T2}, S_{T1}, A_{T2}, A_{T1}, A_{\mathcal{K}},$

$B = \{(x_{min}, x_{max}), (y_{min}, y_{max}), (z_{min}, z_{max})\}, v_s, \{P_i\}_{i=1}^2.$

Ensure: Segmentation map S_M with the classification into background, CSF, UWM, CGM and SGM.

GM zone enhancing

$S_M \leftarrow CGMEnhancing(S_{T2}, A_{\mathcal{K}}, B, v_s, P_1).$

$S_M \leftarrow SGMEnhancing(S_M, S_{T2}, S_{T1}, A_{T2}, A_{T1}, A_{\mathcal{K}}, B, P_2).$

IV.1 GM zone enhancing

IV.1.1 CGM enhancing

The input to this GM enhancing step is the subject T2 preprocessed MRI image S_{T2} , the aligned atlas labels image $A_{\mathcal{K}}$, the bounding box coordinates of the IC mask $B = \{(x_{min}, x_{max}), (y_{min}, y_{max}), (z_{min}, z_{max})\}$, the physical voxel spacing in millimeters v_s and the set of parameters $P_1 = \{\gamma, \tau\}$, where each parameter can be in the range $(0, 1]$. The following variables are now defined and used in this chapter to denote voxel indices as follows:

$$r \stackrel{\text{def}}{=} (x, y, z),$$

$$p \stackrel{\text{def}}{=} (x_1, y_1, z_1),$$

$$r_1 \stackrel{\text{def}}{=} (x_1, y_1, z),$$

where r_1 is used to index voxels at slice z .

In order to produce a CGM mask image that is highly likely to contain all of the true CGM voxels, a preliminar mask image M_p is first produced by setting as 1 (foreground) those voxels where the registered atlas labels indicate CGM tissue and as 0 (background) the rest of the voxels in the volume. Then, a morphological dilation is carried out on M_p to produce the new CGM mask image M_{CGM} as follows:

$$M_{CGM}(r) = \delta_{B_\eta} [M_p](r) \quad \forall r \in \Omega \quad (2)$$

where $\Omega = \{p : x_{min} \leq x_1 \leq x_{max}, y_{min} \leq y_1 \leq y_{max}, z_{min} \leq z_1 \leq z_{max}\}$ is the subject image domain. The morphological dilation and the structuring element B_η are defined as in chapter III in section III.1. The diameter value η of the sphere structuring element depends on a known typical CGM thickness value in the human brain. In this regard, (Shi et al., 2009) reported that the CGM tissue around the WM has a typical minimum thickness value of 1.5 millimeters. The value η is automatically set as follows:

$$\eta = \left\lceil \frac{1.5}{v_s} \right\rceil + 1 \quad (3)$$

where v_s is the physical spacing in millimeters that each isotropic voxel represents. The value of 1 is added to the diameter because the origin of the structuring element occupies one voxel unit which is not considered for the morphological dilation operation. Figure IV.2 shows two coronal slices of the resulting CGM mask image M_{CGM} corresponding to the first and second subject training volumes respectively and their comparison with the corresponding non-dilated masks.

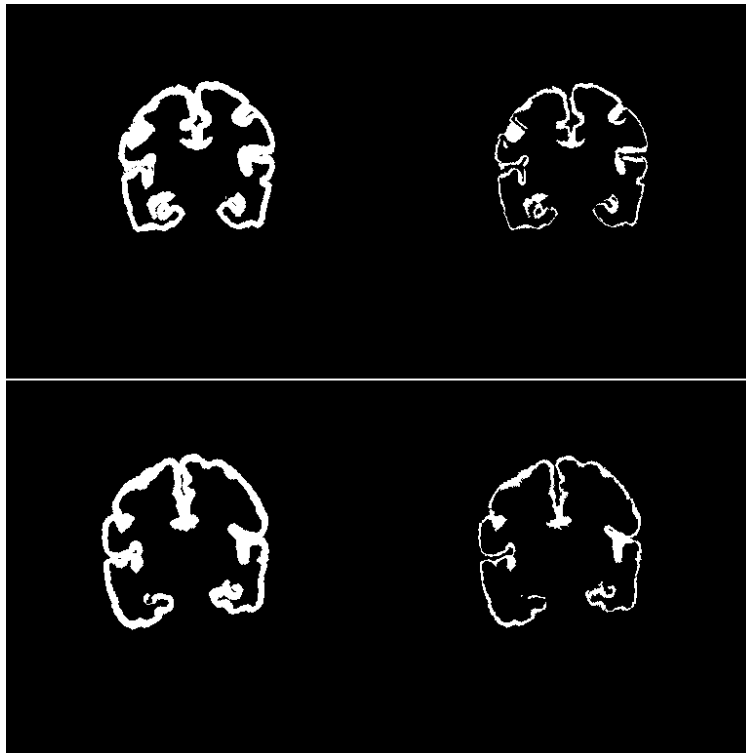


Figure IV.2: Coronal slices showing the result of the dilated CGM mask and its comparison with the corresponding non-dilated mask for the first and second subject training volumes. All images correspond to subjects at 30 weeks of corrected age. The top row corresponds to the first training volume while the bottom row corresponds to the second training volume. *Left column:* dilated CGM masks. *Right column:* non-dilated CGM masks.

A Hessian filter is then considered for enhancing the CGM tissue without depending only on the registered atlas labels information. The Hessian filter H_1 , originally proposed by (Frangi, Niessen, Vincken, & Viergever, 1998) and adapted by (Shi et al., 2009) to generate improved CGM priors, has the following formulation:

$$H_1(r) = \max \{V_L(r), V_P(r)\} \quad \forall r \in I \quad (4)$$

where

- I is the subject MRI image domain,
- $V_L(r)$ indicates a line-like structure filter evaluated at voxel r ,
- $V_P(r)$ indicates a plate-like structure filter evaluated at voxel r .

$V_L(r)$ and $V_P(r)$ are defined as follows:

$$V_L(r) = \begin{cases} \left(1 - \exp\left(-\frac{R_A(r)^2}{2\alpha^2}\right)\right) D(r), & \text{if } cond_1, \\ 0, & \text{otherwise,} \end{cases} \quad (5)$$

$$V_P(r) = \begin{cases} \exp\left(-\frac{R_A(r)^2}{2\alpha^2}\right) D(r), & \text{if } cond_2, \\ 0, & \text{otherwise,} \end{cases} \quad (6)$$

with

$$cond_1 \stackrel{\text{def}}{=} \begin{cases} \lambda_2(r) < 0 \text{ and } \lambda_3(r) < 0, & \text{if the filter is applied on a T1 image,} \\ \lambda_2(r) > 0 \text{ and } \lambda_3(r) > 0, & \text{if the filter is applied on a T2 image,} \end{cases} \quad (7)$$

$$cond_2 \stackrel{\text{def}}{=} \begin{cases} \lambda_3(r) < 0, & \text{if the filter is applied on a T1 image,} \\ \lambda_3(r) > 0, & \text{if the filter is applied on a T2 image,} \end{cases} \quad (8)$$

$$D(r) = \exp\left(-\frac{R_B(r)^2}{2\beta^2}\right) \left(1 - \exp\left(-\frac{S(r)^2}{2c^2}\right)\right), \quad (9)$$

$$R_A(r) = \frac{|\lambda_2(r)|}{|\lambda_3(r)|}, \quad R_B(r) = \frac{|\lambda_1(r)|}{\sqrt{|\lambda_2(r)\lambda_3(r)|}}, \quad S(r) = \sqrt{\sum_{j=1}^3 \lambda_j(r)}, \quad (10)$$

and where

$\lambda_i(r) \forall i \in \{1, 2, 3\}$ are the eigenvalues associated with the 3x3 Hessian matrix evaluated at the r voxel, such that $|\lambda_1(r)| \leq |\lambda_2(r)| \leq |\lambda_3(r)|$,
 α, β, c are the parameters that control the structure sensitivity of the filter.

In this thesis work equation (4) is considered but with the following logarithmic scaling to produce the filter H_2

$$H_2(r) = \begin{cases} Z \left[\ln(\max\{H_1(r), \epsilon\}) - \ln(\epsilon) \right], & \text{if } M_{CGM}(r) = 1 \\ 0, & \text{otherwise} \end{cases} \quad (11)$$

with

$$Z = -\frac{1}{\ln(\epsilon)},$$

and where ϵ is a small constant below of which the values of $H_1(r)$ are taken to be zero. By first defining the following variables

$$\begin{aligned} m_{R_A} &\stackrel{\text{def}}{=} \max_{r \in \Omega} \{R_A(r)\}, \\ m_{R_B} &\stackrel{\text{def}}{=} \max_{r \in \Omega} \{R_B(r)\}, \\ m_S &\stackrel{\text{def}}{=} \max_{r \in \Omega} \{S(r)\}, \end{aligned}$$

then, the free parameters α , β and c are set as follows in order to depend only on the parameter γ

$$\begin{aligned} \alpha &= \gamma m_{R_A}, \\ \beta &= \gamma m_{R_B}, \\ c &= \gamma m_S, \end{aligned}$$

where $\gamma \in (0, 1]$ is a proportion that controls how fast the response of each exponential function in the Hessian filter decays over the spatial signal of the image. It is recommended that ϵ is set with a value that complies with the following

$$\epsilon \leq \min\{a, b\}ab, \tag{12}$$

with

$$a = 1 - \exp\left(-\frac{1}{2\gamma^2}\right),$$

and

$$b = \exp\left(-\frac{1}{2\gamma^2}\right).$$

Inequality (12) should be applied strictly if it is desired that the full range of the filter output is considered. However, a small enough value for ϵ up to the machine precision used can also be considered because the γ parameter has a higher impact on the filter response than a small enough ϵ value.

The reason for the logarithmic scaling in equation (11) of the original filter proposed by (Shi et al., 2009) is because it was observed that the unscaled filter response produced various undesirable discontinuities in the detected CGM structures. By applying the logarithm to the original filter response, the dynamic range of the produced image is compressed enhancing the previous low voxel intensity values where the undesirable discontinuities were present. The rest of the elements in equation (11) are there to ensure that the output is normalized to $[0, 1]$. In the segmentation framework, equation (11) is applied to the infant subject T2 image because better results were observed by using only the T2 image (see chapter V in the Segmentation - CGM enhancing subsection). Equation (11) produced good results in most of the CGM zones with some exceptions. Those exceptions are the regions of CGM that are less line-like and thin are more blobby-like and thick in the available manually segmented infant MRI images. In this regard, it is mentioned in (Chudler, 2015) that the sulci (singular sulcus) are the grooves in the surface of the brain (cerebral cortex), while the gyri (singular gyrus) are the ridges between the

sulci. Also, a fissure is a groove deeper than a sulcus. Examples of more blobby-like and thicker CGM regions that are not well detected by the Hessian filter response from equation (11) are shown in Figure IV.3. Furthermore, in (Ribas, 2010) it is mentioned that fissures, sulci and gyri characterize the currently accepted human cortical brain pattern. Because of the previous reasons a more in-depth study of the geometrical properties of fissures, sulci and gyri in the brain is recommended in this thesis work to enhance the segmentation results of the CGM (see chapter VI). However a further enhancement at the fissure zones in the CGM that deals with this problem with the help of a 2D box filter B_f is also proposed here as follows (applied independently to each coronal slice z_1):

$$F_{CGM}(x_1, y_1, z_1) = \sum_{x_2=-\lfloor \frac{\eta}{2} \rfloor}^{\lfloor \frac{\eta}{2} \rfloor} \sum_{y_2=-\lfloor \frac{\eta}{2} \rfloor}^{\lfloor \frac{\eta}{2} \rfloor} B_f(x_1 - x_2, y_1 - y_2) h_{CGM}(x_2, y_2, z_1) \quad \forall x_1, y_1, z_1 \quad (13)$$

where

$$h_{CGM}(x, y, z) = \begin{cases} 1, & \text{if } A_{\mathcal{K}}(x, y, z) = k_4, \\ 0, & \text{otherwise,} \end{cases} \quad (14)$$

and

$$B_f(x, y) = \begin{cases} \frac{1}{\eta^2}, & \text{if } -\lfloor \frac{\eta}{2} \rfloor \leq x, y \leq \lfloor \frac{\eta}{2} \rfloor, \\ 0, & \text{otherwise,} \end{cases} \quad (15)$$

The previous means that B_f also depends on the minimum known typical CGM thickness value of 1.5 millimeters reported by (Shi et al., 2009) because its window size is equal to the sphere structuring element diameter η .

The final CGM zone is computed by first initializing a seed with both the fissure zone enhancement function from (13) and the Hessian filter information from (11). A region growing algorithm is then applied as a post-processing step to that initial CGM seed. The auxiliary memory V_{CGM} and a seed U_{CGM} are computed as follows to aid both in the region growing algorithm:

$$V_{CGM}(r) = \begin{cases} 1, & \text{if } \frac{H_2(r) + F_{CGM}(r)}{2} > \tau \\ 0, & \text{otherwise,} \end{cases} \quad (16)$$

$$U_{CGM}(r) = \begin{cases} 1, & \text{if } V_{CGM}(r) = 1 \text{ and } M_{CGM}(r) = 1 \\ 0, & \text{otherwise,} \end{cases} \quad (17)$$

where the code 1 in $V_{CGM}(r)$ indicates a candidate code for CGM.

Algorithm 2 is a region growing algorithm whose purpose is to expand the initial CGM zone in the U_{CGM} seed at regions possibly mislabeled that are outside the M_{CGM} mask. Algorithm 2 is applied slice by slice depending on how the subject

image was scanned. For the case of the (NeoBrainS12, 2012) challenge data used in this thesis work, the algorithm was applied along each coronal slice.

As a next post-processing step of the CGM enhancing stage, Algorithm 3 is applied to label the S_M segmentation map according to the output U_{CGM} from Algorithm 2 and to the registered atlas labels $A_{\mathcal{K}}$. In both Algorithm 2 and Algorithm 3, $\mathcal{N}_d(r)$, with $d = 1$ is defined as follows:

$$\mathcal{N}_d(r) = \{r_1 \in \Omega \mid \|r_1 - r\|^2 \leq d\} \quad (18)$$

which indicates indexes of a local neighbourhood of voxel r at slice z . Specifically, $\mathcal{N}_1(r)$ indicates the four first order indexes of the neighbours of voxel r . Also, in Algorithm 3 the $h_{\mathcal{K}}$ function used is defined as follows:

$$h_{\mathcal{K}}(r, k) = \begin{cases} 1, & \text{if } A_{\mathcal{K}}(r) = k. \\ 0, & \text{otherwise} \end{cases} \quad (19)$$

where $k \in \mathcal{K}$. In case of ties in the neighbours $\mathcal{N}_1(r)$ in the last sentence of Algorithm 3, CSF (k_2) takes priority, then UWM (k_3), and then SGM (k_4), which allows to decide a label for $S_M(r)$.

Algorithm 2 Region growing algorithm for the U_{CGM} CGM seed.

Require: U_{CGM}, V_{CGM} ,

$$B = \{(x_{min}, x_{max}), (y_{min}, y_{max}), (z_{min}, z_{max})\}.$$

Ensure: Grown CGM zone stored in U_{CGM} and indicated by the code 1.

```

for every slice  $z \in [z_{min}, z_{max}]$  {
  do {
     $candidateList \leftarrow \emptyset$ .
    for every voxel index  $r \in \Omega$  at slice  $z$  {
      if  $U_{CGM}(r) = 1$  {
        for  $r_1 \in \mathcal{N}_1(r)$  {
          if  $U_{CGM}(r_1) = 0$  and  $V_{CGM}(r_1) = 1$  {
             $candidateList \leftarrow candidateList \cup \{r_1\}$ .
          }
        }
      }
    }
    for every voxel index  $r_1 \in candidateList$  {
       $U_{CGM}(r_1) \leftarrow 1$ .
       $V_{CGM}(r_1) \leftarrow 2$ .
    }
  } while ( $candidateList \neq \emptyset$ )
}

```

Algorithm 3 Final labeling step of the CGM enhancing stage.

Require: $A_{\mathcal{K}}, U_{CGM}$,

$$B = \{(x_{min}, x_{max}), (y_{min}, y_{max}), (z_{min}, z_{max})\}.$$

Ensure: Segmentation map S_M with the classification into background, CSF, UWM, CGM and SGM.

```

for every voxel index  $r \in \Omega$  {
     $S_M(r) \leftarrow k_1$ .
    if  $U_{CGM}(r) = 1$  {
         $S_M(r) \leftarrow k_4$ .
    } else if  $A_{\mathcal{K}}(r) = k_2$  or  $A_{\mathcal{K}}(r) = k_5$  {
         $S_M(r) \leftarrow A_{\mathcal{K}}(r)$ .
    } else {
         $S_M(r) \leftarrow \underset{k \in \{k_2, k_3, k_4\}}{\operatorname{argmax}} \sum_{r_1 \in \mathcal{N}_1(r)} h_{\mathcal{K}}(r_1, k)$ .
    }
}

```

As a final post-processing step, the voxels with a different label from CSF that are in a Connected Component (CC) surrounded by CSF are corrected. For this a binary mask is computed by setting as 0 those voxels in the volume labeled as CSF and as 1 the rest of the voxels. After the previous, the Connected Components (CCs) of the binary mask are computed (on the regions labeled as 1) and if a voxel does not belong to the largest CC, then it is labeled as CSF. The previous ensures that if there are CCs inside of CSF regions, they are labeled as CSF, getting rid that way of possible brain tissues mislabeled inside the CSF.

The parameters γ and τ were set as 0.3 and 0.3 respectively (see the Segmentation - CGM enhancing subsection in chapter V for the justification). Figure IV.3 shows coronal slices depicting the CGM enhancing step applied on the training T2 preprocessed image volumes of the infant subjects.

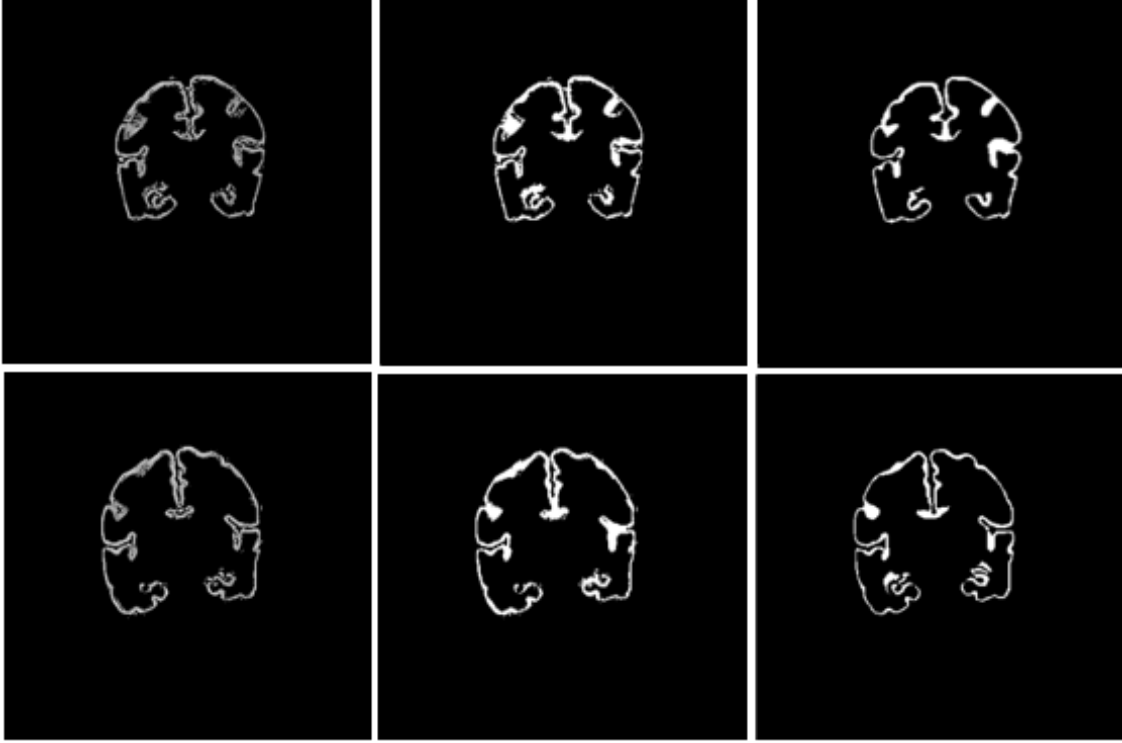


Figure IV.3: Coronal slices showing the comparison between two steps in the CGM enhancing process applied to the T2 preprocessed images and the manual segmentation of the CGM corresponding to the same slice. All images correspond to subjects at 30 weeks of corrected age. The top row corresponds to the first training volume while the bottom row corresponds to the second training volume. *Left column*: result of the Hessian filter applied to the T2 images (the response is in grayscale). *Middle column*: final result of the CGM enhancing step (binarized). *Right column*: manual segmentation of the CGM tissue (binarized).

IV.1.2 SGM enhancing

The input to this GM enhancing step is the subject T1 and T2 preprocessed MRI images S_{T1} and S_{T2} , the aligned atlas labels image $A_{\mathcal{K}}$, the atlas T1 and T2 images A_{T1} and A_{T2} , the segmentation map that was the output of the CGM enhancing step S_M , the bounding box coordinates of the IC mask $B = \{(x_{min}, x_{max}), (y_{min}, y_{max}), (z_{min}, z_{max})\}$ and the set of parameters $P_2 = \{nl, nnl, w, ps\}$.

For the refinement of the GM at the SGM zone, which is taken as the voxels labeled as SGM (k_5) in $A_{\mathcal{K}}$, local and non-local 2D neighbourhoods in each coronal slice are taken to define the probability of a voxel of belonging to each class based on the labels in $A_{\mathcal{K}}$ on those neighbourhoods. The class with highest probability is then taken as the label of that voxel. The probability of a voxel r of belonging to a class $k \in \mathcal{K}$ in the SGM zone is computed as follows

$$P_k(r) = \frac{\sum_{r_1 \in \mathcal{N}_S^N(r)} h_{\mathcal{K}}(r_1, k) + \sum_{r_1 \in \mathcal{N}_d(r)} h_{\mathcal{K}}(r_1, k)}{\#\mathcal{N}_S^N(r) + \#\mathcal{N}_d(r)} \quad (20)$$

$$\forall r \in \{p \mid A_{\mathcal{K}}(p) = k_5\}$$

where $h_{\mathcal{K}}$ is the same function defined in (19), $d = 1$ when the number of local neighbours $nl = 4$, $d = 2$ when $nl = 8$, and

$$\mathcal{N}^N(r) = \left\{ r_1 \in \{\mathcal{N}_a(r) \setminus \mathcal{N}_d(r)\} \mid a = 2 \left\lfloor \frac{w}{2} \right\rfloor^2, d = \{1, 2\} \right\}, \quad (21)$$

where $\mathcal{N}^N(r)$ is the index set of a 2D non-local neighbourhood in a squared window of size w by w with $w > 3$ and excluding the local neighbourhood $\mathcal{N}_d(r)$. Then a subset of $\mathcal{N}^N(r)$ is taken, namely $\mathcal{N}_S^N(r)$, which keeps only the most similar nnl voxel indexes in the neighbourhood set. The similarity measure is considered between a patch centered at a neighbouring voxel in the neonate images S_{T1} and S_{T2} and a patch centered at the same neighbouring voxel in the atlas images A_{T1} and A_{T2} respectively. Each patch is defined as follows:

$$M(r) = \begin{bmatrix} Q_{T1}(r) \\ Q_{T2}(r) \end{bmatrix}, \quad (22)$$

where

- $Q_{T1}(r)$: is a 2D ps by ps patch over the coronal slice z vectorized and centered at voxel r in the T1 image modality;
- $Q_{T2}(r)$: is a 2D ps by ps patch over the coronal slice z vectorized and centered at voxel r in the T2 image modality.

Then, the patch similarity between a patch in the subject images and a patch in the atlas images is defined as follows:

$$PS(M_S(r), M_A(r)) = M_S(r)^T M_A(r), \quad (23)$$

where

- $M_S(r)$: is the patch in the subject images;
- $M_A(r)$: is the patch in the atlas images.

The set in $\mathcal{N}_S^N(r)$ denotes the same 2D non-local neighbourhood as the set in (21) but keeping only those neighbours that fulfill a patch-based similarity criterion. The similarity criterion used in $\mathcal{N}_S^N(r)$ consists of keeping only the the nnl neighbours with the highest dot product between each considered vectorized patch.

It was experimentally observed that reducing the considered non-local neighbours in the set $\mathcal{N}^N(r)$ to only 50% and picked at random before computing the $\mathcal{N}_S^N(r)$ set improved the results (see the Segmentation - SGM enhancing subsection in chapter V). Therefore, the SGM enhancing step considers only 50% of the neighbours in the non-local neighbourhood from the set in (21). The parameters nl, nnl, w and ps were set as 8, 6, 7 and 3 respectively (see the Segmentation - SGM enhancing subsection in chapter V for the justification). Figure IV.4 shows coronal slices comparing the segmentation results between the two GM enhancing steps and the manual segmentation.

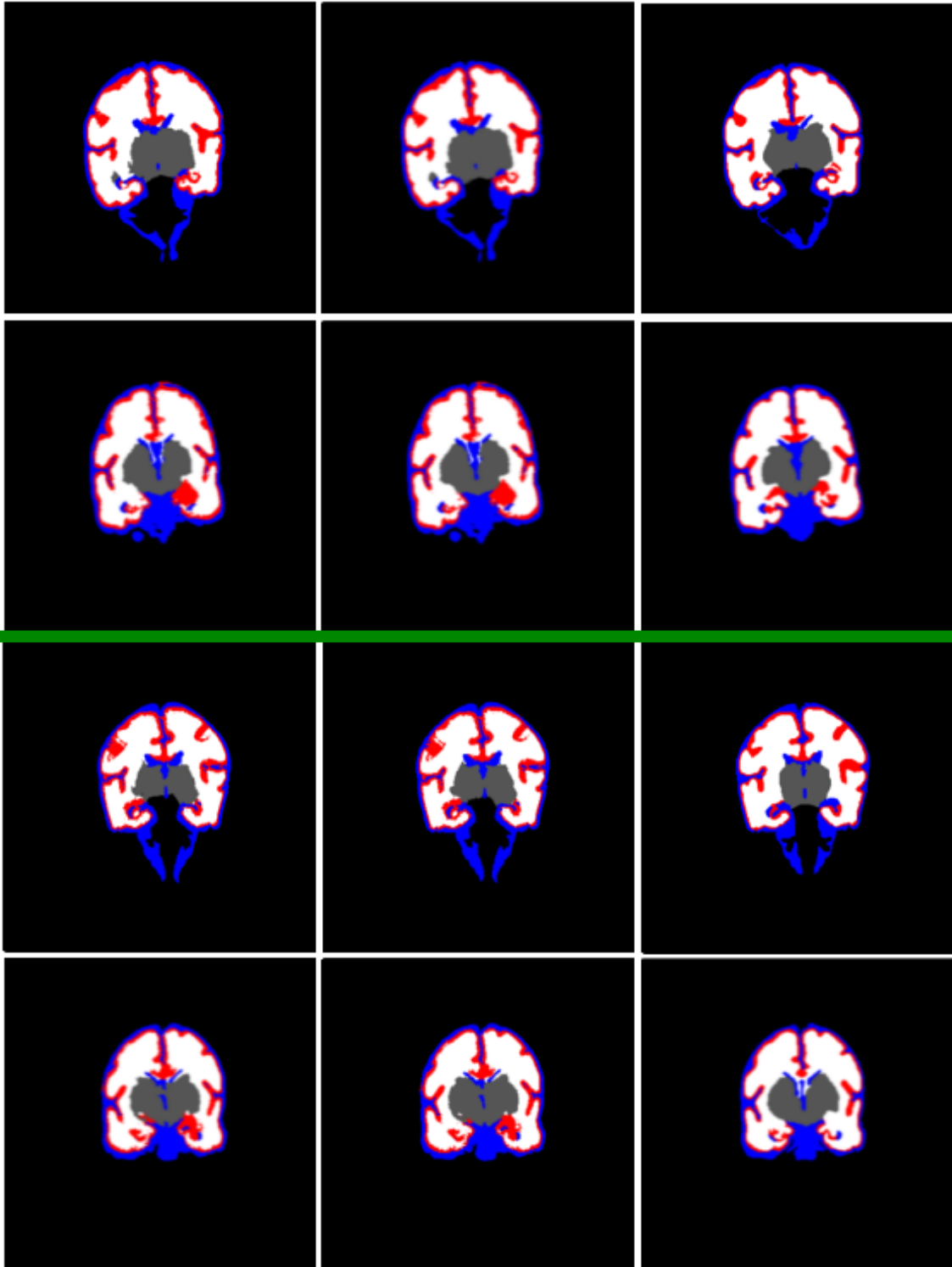


Figure IV.4: Coronal slices showing the comparison between the segmentation achieved until the CGM enhancing, the SGM enhancing and also the manual segmentation. All images correspond to subjects at 30 weeks of corrected age. The rows above the green line correspond to the second training volume while the rows below the green line correspond to the first training volume. *Left column*: result of the segmentation until the CGM enhancing step. *Middle column*: result of the segmentation until the SGM enhancing step. *Right column*: manual segmentation (ground truth). The blue color indicates CSF, the red color indicates CGM, the gray color indicates SGM and the white color indicates UWM.

Chapter V

Experiments and discussion of the results

This chapter presents experiments made in order to perform tuning of the parameters considered at the segmentation stage and in order to justify using specific data or applying specific steps during various stages of the segmentation framework. All the experiments presented in this chapter were made by using data from the 30 weeks coronal set of the (NeoBrainS12, 2012) challenge, which consists of five volumes for testing and two volumes for training. The data was taken from <http://neobrain12.isi.uu.nl>. Each volume includes a T1 and T2 image modality and in the case of the training volumes the manual segmentation is also included. The two training volumes with their manual segmentations were used for the tuning of the parameters.

First, one of the training volumes was used as the input subject and the remaining training volume as the infant brain atlas. Then the previous step was repeated but switching the role of each input training volume and the average across both results was taken. It is also presented (in this chapter) the segmentation results obtained by using the segmentation framework proposed in this work on the 30 weeks corrected age coronal set of the (NeoBrainS12, 2012) challenge.

Two measures were used to perform the tuning of the parameters. First, the Dice coefficient (Dice, 1945), which is defined as follows in the context of this segmentation framework:

$$Dice = \frac{2\#\{X_A \cap X_B\}}{\#X_A + \#X_B} \quad (24)$$

where X_A refers to the set of voxels corresponding to one of the classes segmented by the framework and X_B refers to the set of voxels corresponding to the manual segmentation of the same class. Second, the overall accuracy (Liu, Frazier, & Kumar, 2007) is defined as follows (also in the context of this segmentation framework):

$$OA = \frac{\sum_{k \in \mathcal{K}} C_{kk}}{\sum_{k \in \mathcal{K}} G_k} \quad (25)$$

where $\mathcal{K} = \{k_2, k_3, k_4, k_5\}$, and k_2, k_3, k_4, k_5 correspond to the CSF, UWM, CGM and SGM classes respectively. G_k denotes the total number of voxels labelled with

class k and C_{kk} denotes the number of voxels having manual segmentation class label $k \in \mathcal{K}$ and also segmentation class label $k \in \mathcal{K}$ resulted from the segmentation framework. In other words, OA measures the proportion of correctly labelled voxels.

V.1 Preprocessing - Intracranial Cavity Extraction

In order to test the quality of the morphology based ICE, the Dice coefficient of the resulting IC in the two training volumes of the 30 weeks corrected age coronal set was compared in two scenarios. In the first scenario, isotropic voxel scaling before the ICE step was considered, and in the second scenario isotropic voxel scaling was not considered. The resulting average Dice coefficient of this experiment under the two scenarios is shown in Table V.1. The results are rounded to 5 decimal digits.

It can be observed in Table V.1 that by using isotropic voxel scaling (yellow column), the result improves more than 0.02 in average Dice coefficient, which is a considerable amount. This is the reason that isotropic voxel scaling was not discarded as a preprocessing step before the ICE in the segmentation framework.

	Isotropic voxels	
	True	False
Average Dice	0.97688	0.95596

Table V.1: Average Dice coefficient of the IC with and without isotropic voxels for the two training volumes of the 30 weeks corrected age coronal set.

V.2 Preprocessing - Registration

The following experiment was carried out for comparing the quality of both the affine and diffeomorphic registration after the ICE step when different image modalities, T1 and T2, are used for the registration. For this purpose label propagation of the registered atlas on the subject space was used to segment each subject training volume from the 30 weeks corrected age coronal set. The latter was applied while varying the type of registered image modalities. The resulting average Dice coefficient for each segmented class and for each type of image modality registration is shown in Table V.2. The results are rounded to 5 decimal digits.

It can be observed in Table V.2 that in the case of the T2 to T2 image modality registration (yellow column) a better average Dice coefficient was obtained consistently for all the segmented classes. This is the reason that the T2 image modalities are used for both the affine and diffeomorphic registration steps carried out after the ICE to align the atlas to the subject space in the segmentation framework.

	Registration			
	T2 to T2	T1 to T2	T2 to T1	T1 to T1
Avg. CGM Dice	0.67255	0.36700	0.36328	0.51462
Avg. SGM Dice	0.87436	0.86385	0.85626	0.86058
Avg. UWM Dice	0.93343	0.84647	0.86109	0.90015
Avg. CSF Dice	0.82500	0.68900	0.65588	0.74093

Table V.2: Average Dice coefficient for each segmented class (CGM, SGM, UWM and CSF) for the two training volumes of the 30 weeks corrected age coronal set varying the image modalities used for the affine and diffeomorphic registration steps after the ICE.

V.3 Segmentation - CGM enhancing

Tuning of the parameters γ and τ used at the CGM enhancing step was made with the following experiment. With the experiment it was measured, while varying the γ and τ parameter values, the average Dice coefficient segmentation results and the average OA segmentation results across both subject training volumes of the 30 weeks corrected age coronal set. For the experiment, it was considered for each volume the average across all four segmented classes and it was also considered the case of the segmentation of the CGM class alone across both subject training volumes while varying the γ and τ parameters. During this experiment, it was also compared if the quality of the resulting segmentation in this step is better by considering both the T1 and T2 subject image modalities or by considering only the T2 subject image modality. First, Figure V.1 shows as heat maps the average OA across both training volumes considering all four classes while varying the γ and τ parameters. Two cases are shown in Figure V.1, that is when only the T2 preprocessed subject image is present and then when both the T1 and T2 preprocessed subject images are present. Then, Figure V.2 shows as heat maps the average Dice coefficient, across both training volumes, of the average Dice coefficient across all four classes in each training volume while varying the γ and τ parameters. The same two cases considered in Figure V.1 are also considered in Figure V.2. Lastly, Figure V.3 shows as heat maps the average Dice coefficient, across both training volumes, of the Dice coefficient of the CGM class in each training volume while varying the γ and τ parameters. The same two cases considered in Figure V.1 and Figure V.2 are also considered in Figure V.3.

Two things are clearly noticeable in Figures V.1, V.2 and V.3. First, in all cases using only the T2 preprocessed subject image yielded higher maximum average OA and average Dice coefficient values (visible through the scale bar at the right of each heat map). Second, in all cases, among the tested τ parameter values, higher average OA and average Dice coefficient results (because of whiter colors) were achieved with the τ value of 0.3. Focusing now on the case of using only the T2 preprocessed subject image (shown at the top in each figure) and on the row corresponding to the τ value of 0.3 the γ parameter is now inspected. Considering the latter, it can be observed in Figure V.1 that, among the tested γ parameter values, higher average OA was achieved with the γ value of 0.1. Figure V.2 also shows a higher (average

Dice) value for the γ value of 0.1, only T2 image case and τ value of 0.3, although it is difficult to perceive because of the very similar result obtained with the γ value of 0.3. The precise average Dice value shown in the top heat map at the τ value of 0.3 on Figure V.2 corresponds to 0.8459314 when $\gamma = 0.1$ and 0.8458702 when $\gamma = 0.3$. On the other hand, Figure V.3 shows a higher average Dice value of the CGM class for the γ value of 0.3, only T2 image case and τ value of 0.3. The latter is difficult to perceive because of the very similar result obtained with the γ values of 0.5 and 0.7. The precise average Dice value for the CGM class shown in the top heat map at the τ value of 0.3 on Figure V.2 corresponds to 0.7434073 when $\gamma = 0.3$, 0.74121675 when $\gamma = 0.5$ and 0.7390406 when $\gamma = 0.7$. Furthermore, Figure V.4 shows a comparison of CGM segmentation results using different values for the τ and γ parameters. It can be noticed in Figure V.4 that the segmentation is more sensitive to the τ parameter than to the γ parameter. Also, when comparing the first and third column images (from left to right) from Figure V.4 corresponding to $\gamma = 0.1$ and $\gamma = 0.3$, it can be observed that a lower γ value results in a worst CGM detection at very thin regions, for instance, at the sulcal regions.

Since the CGM is very thin in the neonate brain compared to the other tissues that are considered in this work, a higher Dice value specifically for the CGM class is prioritized over the average Dice value over the four considered classes. Furthermore, it should be noted that, although a γ value of 0.1 yields a higher average Dice value over the four considered classes, it has a very small difference with the case of a γ value of 0.3 (less than 1×10^{-4} in average Dice coefficient). For those reasons, the parameters for the CGM enhancing step in the segmentation framework were set as $\tau = 0.3$, $\gamma = 0.3$ and it was decided to use only the T2 preprocessed subject image at this enhancing step.

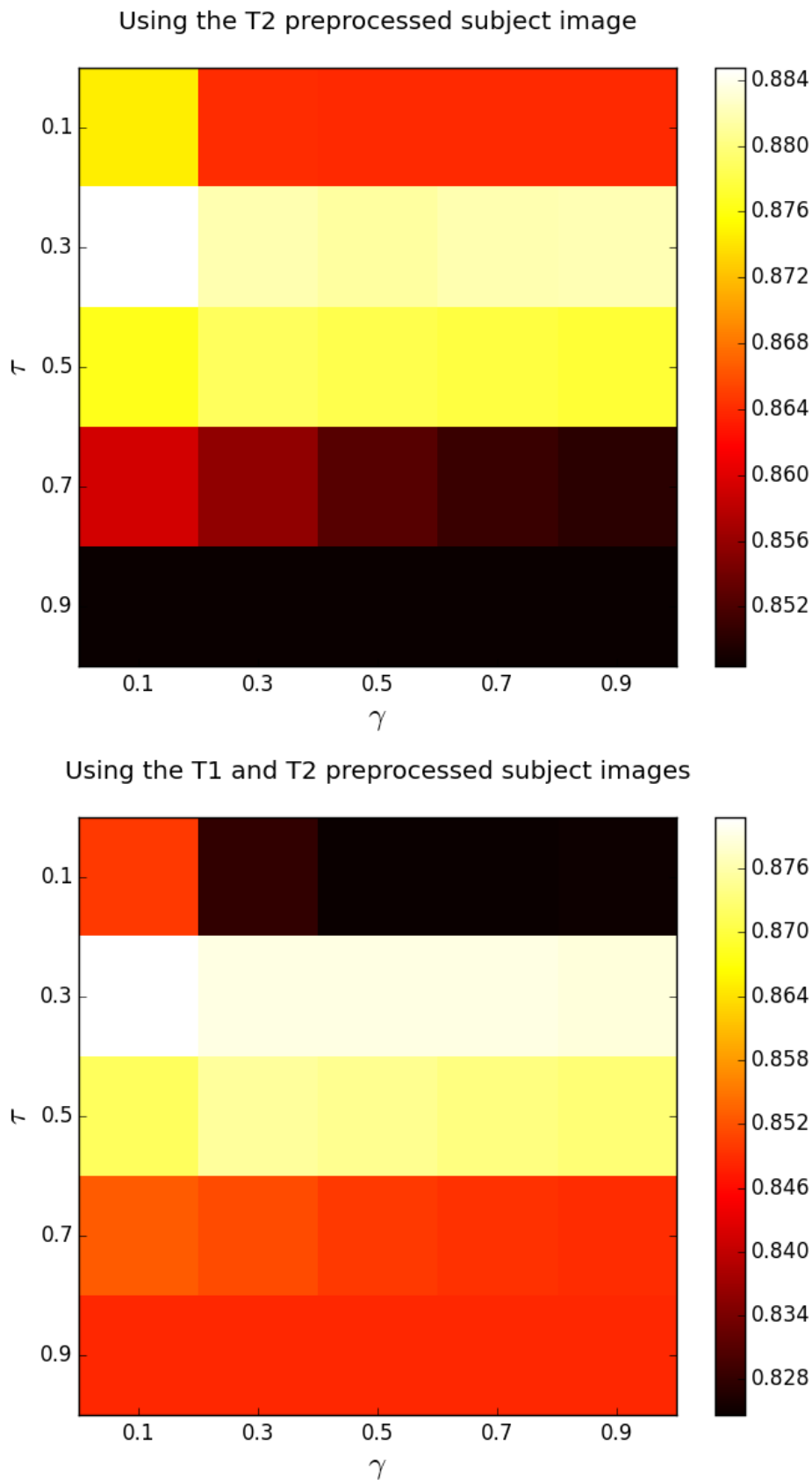


Figure V.1: Heat maps with the average OA , across the two subject training volumes from the 30 weeks corrected age coronal set, of the four segmented classes varying the γ parameter, the τ parameter and considering using only the T2 preprocessed subject image (top) and also using both the T1 and T2 preprocessed subject images (bottom).

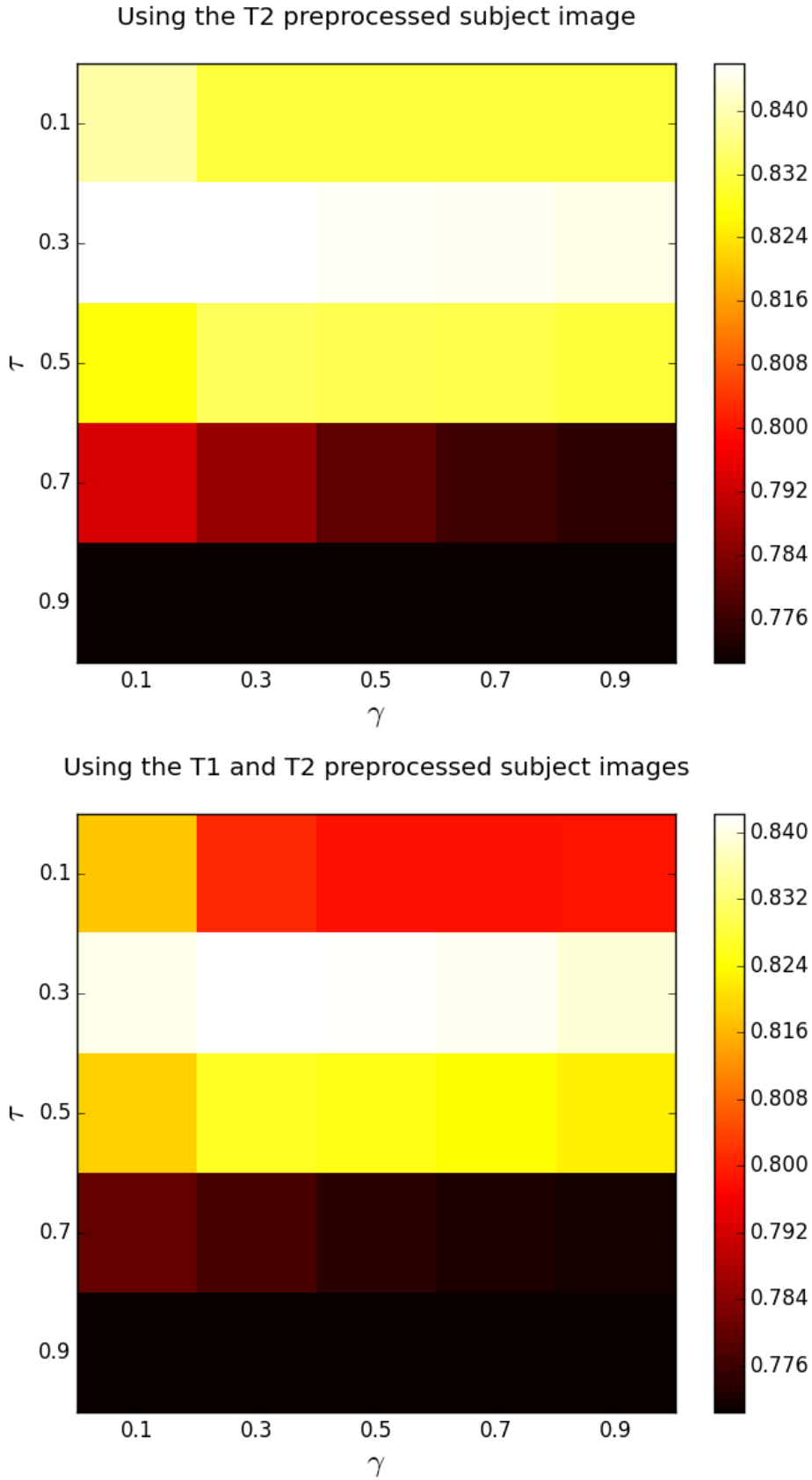


Figure V.2: Heat maps with the average Dice coefficient, across the two subject training volumes from the 30 weeks corrected age coronal set, of the four segmented classes varying the γ parameter, the τ parameter and considering using only the T2 preprocessed subject image (top) and also using both the T1 and T2 preprocessed subject images (bottom).

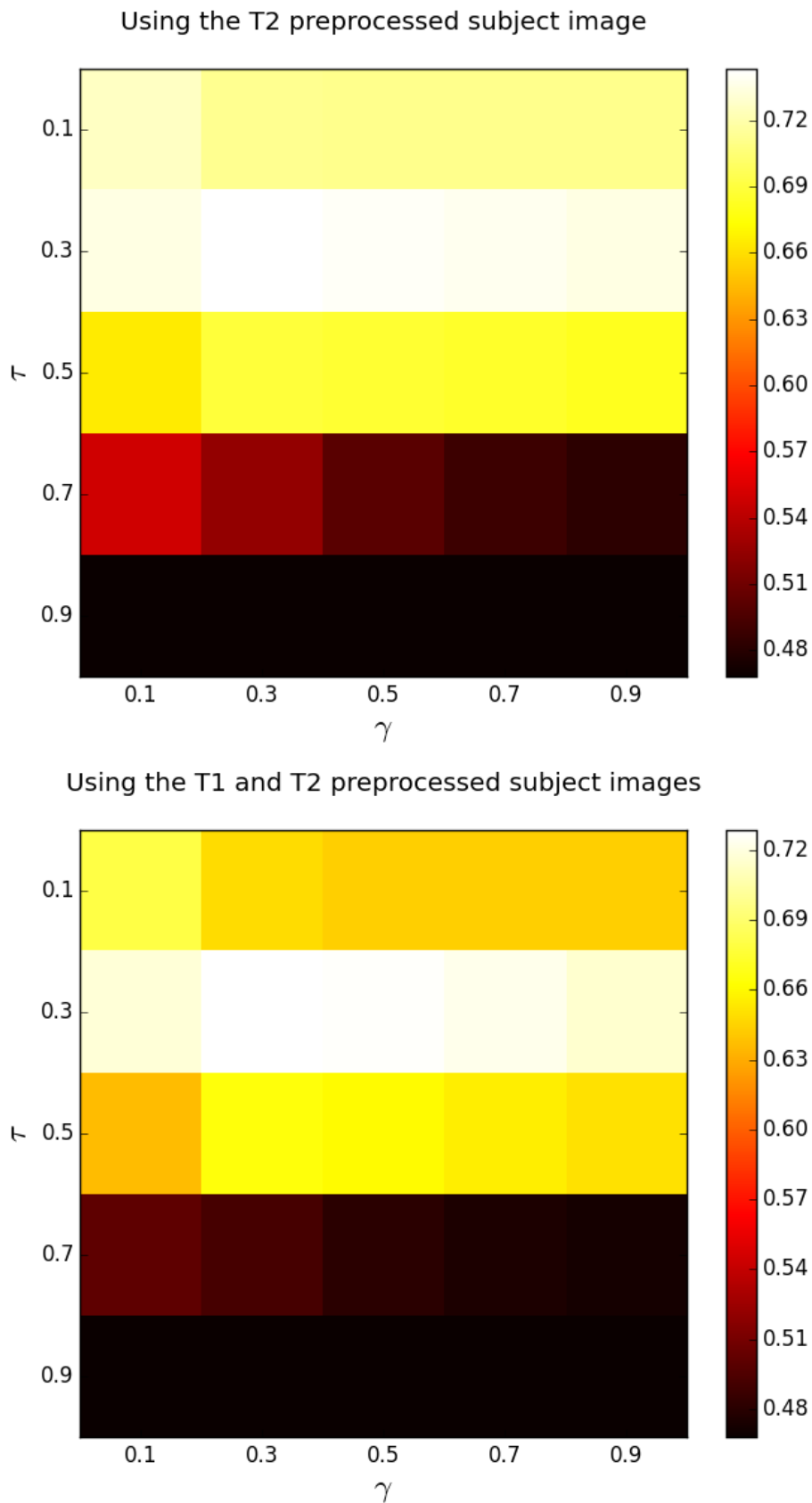


Figure V.3: Heat maps with the average Dice coefficient, across the two subject training volumes from the 30 weeks corrected age coronal set, of the CGM class varying the γ parameter, the τ parameter and considering using only the T2 preprocessed subject image (top) and also using both the T1 and T2 preprocessed subject images (bottom).

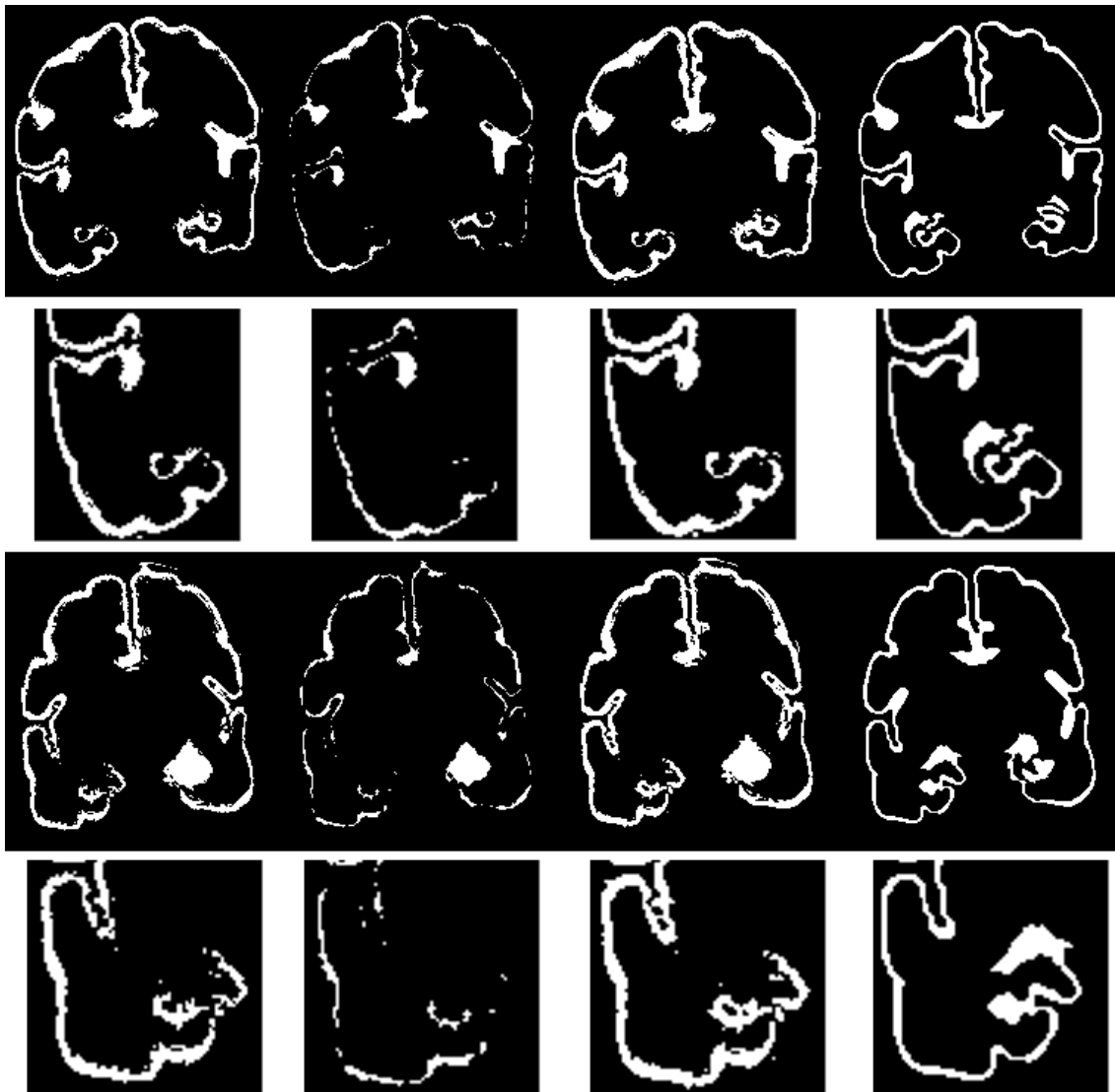


Figure V.4: Coronal slices showing the comparison between the CGM segmentation achieved with different τ and γ parameter values and also the manual CGM segmentation. All images correspond to the second training volume of the 30 weeks corrected age set. From top to bottom, the first and third row correspond to slices without zoom while the second and fourth row correspond to an enlarged portion of the respective previous row images. From left to right, each column corresponds to: $\tau = 0.3$ and $\gamma = 0.1$ (best value in average for τ and worst value in average for γ), $\tau = 0.9$ and $\gamma = 0.3$ (worst value in average for τ and best value in average for γ), $\tau = 0.3$ and $\gamma = 0.3$ (best values in average), and the manual CGM segmentation.

V.4 Segmentation - SGM enhancing

Tuning of the the parameters nl , nml , w and ps used at the SGM enhancing step was made with the following experiment. In the experiment it was measured, while varying the nl , nml , w and ps parameter values, the average Dice coefficient segmentation results and the average OA segmentation results across both subject training volumes of the 30 weeks corrected age coronal set. For this experiment it was also

considered for each volume the average across all four segmented classes. Furthermore, it was also compared if better results were obtained in the case of selecting randomly 50% of the neighbours in the non-local neighbourhood or in the case of no random selection, that is 100% of the neighbours in the non-local neighbourhood.

Table V.3 shows the results of this experiment. It should be noted in particular that in the first row there is one case with 0 values for the parameters and where it was not included the random selection. That case corresponds to not applying the SGM enhancing step and instead it considers only label propagation of the aligned atlas labels. In Table V.3 it can also be noted that there is in general small variation of the resulting average Dice coefficient values and the average *OA* values as the SGM enhancing parameters are varied together with the other case of including and not including the random selection. However, despite the small variation a maximum value for both the average *OA* and the average Dice coefficient can be observed in Table V.3 in the yellow row. Furthermore, when comparing the case when the SGM enhancing step is not considered and the case corresponding to the yellow row in Table V.3 an increase in the Dice coefficient of the SGM class is consistently observed in both training volumes. Specifically, the Dice coefficients of the SGM class when the SGM enhancing step was not used were 0.8688012 for the first subject training volume and 0.8799110 for the second subject training volume. On the other hand, the Dice coefficients of the SGM class that correspond to the yellow row in Table V.3 were 0.8762305 for the first subject training volume and 0.8814488 for the second subject training volume. Furthermore, Figure V.5 shows a comparison of SGM segmentation results of two slices using the worst and the best parameter values found in the experiment, which correspond to the first and second columns from left to right respectively. The results in both cases are visually very similar as already suggested by the results from Table V.3. However a slight improvement using the best parameters can be appreciated in the detection of the small CSF hole inside the SGM on the top row of Figure V.5. In both cases of the top row of Figure V.5 a small SGM CC was incorrectly detected (visible at the left bottom part). Those incorrect detections are mainly due to the great variation in the SGM tissue of the neonates, which means that the results are biased to some degree towards the used atlas.

For the previous reasons, it was decided to include the SGM enhancing step in the segmentation framework and its parameters were set as $nl = 8$, $nnl = 6$, $w = 7$, $ps = 3$ and it was also decided to use only a random selection of 50% of the neighbours in the non-local neighbourhood.

nl	nnl	w	ps	50%random	Avg. Dice	Avg. OA
0	0	0	0	False	0.8263338	0.8630763
4	2	5	3	False	0.8266974	0.8632596
8	2	5	3	False	0.8269517	0.8633908
4	4	5	3	False	0.8271189	0.8634038
8	4	5	3	False	0.8267541	0.8633562
4	6	5	3	False	0.8269517	0.8633908
8	6	5	3	False	0.8266848	0.8633404
4	8	5	3	False	0.8267541	0.8633562
8	8	5	3	False	0.8269102	0.8634205
4	2	7	3	False	0.8266974	0.8632596
8	2	7	3	False	0.8270829	0.8634498
4	4	7	3	False	0.8271189	0.8634038
8	4	7	3	False	0.8267219	0.863361
4	6	7	3	False	0.8270829	0.8634498
8	6	7	3	False	0.8265191	0.863324
4	8	7	3	False	0.8267219	0.863361
8	8	7	3	False	0.8262202	0.863216
4	2	5	5	False	0.8266974	0.8632596
8	2	5	5	False	0.8269517	0.8633908
4	4	5	5	False	0.8271189	0.8634038
8	4	5	5	False	0.8267541	0.8633562
4	6	5	5	False	0.8269517	0.8633908
8	6	5	5	False	0.8266848	0.8633404
4	8	5	5	False	0.8267541	0.8633562
8	8	5	5	False	0.8269102	0.8634205
4	2	7	5	False	0.8266974	0.8632596
8	2	7	5	False	0.8270829	0.8634498
4	4	7	5	False	0.8271189	0.8634038
8	4	7	5	False	0.8267219	0.863361
4	6	7	5	False	0.8270829	0.8634498
8	6	7	5	False	0.8265191	0.863324
4	8	7	5	False	0.8267219	0.863361
8	8	7	5	False	0.8262202	0.863216
4	2	5	7	False	0.8266974	0.8632596
8	2	5	7	False	0.8269517	0.8633908
4	4	5	7	False	0.8271189	0.8634038
8	4	5	7	False	0.8267541	0.8633562
4	6	5	7	False	0.8269517	0.8633908
8	6	5	7	False	0.8266848	0.8633404
4	8	5	7	False	0.8267541	0.8633562
8	8	5	7	False	0.8269102	0.8634205
4	2	7	7	False	0.8266974	0.8632596
8	2	7	7	False	0.8270829	0.8634498
4	4	7	7	False	0.8271189	0.8634038
8	4	7	7	False	0.8267219	0.863361
4	6	7	7	False	0.8270829	0.8634498

nl	nnl	w	ps	50%random	Avg. Dice	Avg. OA
8	6	7	7	False	0.8265191	0.863324
4	8	7	7	False	0.8267219	0.863361
8	8	7	7	False	0.8262202	0.863216
4	2	5	3	True	0.8266581	0.863198
8	2	5	3	True	0.8272326	0.8634602
4	4	5	3	True	0.8268393	0.8632948
8	4	5	3	True	0.8271242	0.8634186
4	6	5	3	True	0.8268244	0.8632901
8	6	5	3	True	0.8272858	0.8634914
4	8	5	3	True	0.8271297	0.8634278
8	8	5	3	True	0.8274749	0.8635714
4	2	7	3	True	0.8267016	0.8632372
8	2	7	3	True	0.827189	0.8634492
4	4	7	3	True	0.826828	0.8632956
8	4	7	3	True	0.8274257	0.8635678
4	6	7	3	True	0.8270803	0.8634155
8	6	7	3	True	0.8274824	0.8635884
4	8	7	3	True	0.827045	0.8634024
8	8	7	3	True	0.8273764	0.8635391
4	2	5	5	True	0.8266433	0.8631946
8	2	5	5	True	0.8270569	0.8633962
4	4	5	5	True	0.8268315	0.8632882
8	4	5	5	True	0.8272127	0.863467
4	6	5	5	True	0.8269343	0.8633362
8	6	5	5	True	0.827338	0.8635194
4	8	5	5	True	0.8270793	0.8634051
8	8	5	5	True	0.8274227	0.8635594
4	2	7	5	True	0.8268018	0.863279
8	2	7	5	True	0.8272826	0.8634744
4	4	7	5	True	0.8268529	0.86331
8	4	7	5	True	0.8272829	0.8635036
4	6	7	5	True	0.8270018	0.8633748
8	6	7	5	True	0.827404	0.8635489
4	8	7	5	True	0.8270271	0.8633862
8	8	7	5	True	0.827476	0.8635824
4	2	5	7	True	0.826666	0.863203
8	2	5	7	True	0.8271437	0.863424
4	4	5	7	True	0.8268569	0.8632938
8	4	5	7	True	0.8272157	0.8634646
4	6	5	7	True	0.8269619	0.86335
8	6	5	7	True	0.8273787	0.8635282
4	8	5	7	True	0.8270927	0.8634112
8	8	5	7	True	0.8274722	0.8635814
4	2	7	7	True	0.8267634	0.8632647
8	2	7	7	True	0.8272045	0.863457
4	4	7	7	True	0.8268945	0.8633209

nl	nnl	w	ps	50%random	Avg. Dice	Avg. OA
8	4	7	7	True	0.8272823	0.8634866
4	6	7	7	True	0.8269608	0.8633605
8	6	7	7	True	0.8274246	0.863567
4	8	7	7	True	0.8271658	0.8634426
8	8	7	7	True	0.8274312	0.8635715

Table V.3: Average OA across the two subject training volumes from the 30 weeks corrected age coronal set and average Dice coefficient, across the same two subject training volumes and also across the four segmented classes as the SGM enhancing parameters are varied. It was also considered the case of including only 50% of the neighbours in the non-local neighbourhood. Both T1 and T2 subject and atlas image modalities were considered.



Figure V.5: Coronal slices showing the comparison between the SGM segmentation achieved with the best and the worst parameter values and also the manual SGM segmentation. All images correspond to the second training volume of the 30 weeks corrected age set. The top row corresponds to one coronal slice while the bottom row corresponds to a different coronal slice. From left to right, each column corresponds to: $nl = 8, nnl = 8, w = 7, ps = 7$ and no random selection (worst parameter values in average), $nl = 8, nnl = 6, w = 7, ps = 3$ and random selection (best parameter values in average), and the manual SGM segmentation.

V.5 NeobrainS12 challenge results

The five subject test volumes from the 30 weeks corrected age coronal set of the (NeoBrainS12, 2012) challenge were segmented with the tuned parameters of the GM enhancing segmentation stage and it was included only the specific information mentioned in the previous sections of this chapter. The individual evaluation results for each test volume are shown in Table V.4. Table V.5 on the other hand shows the average evaluation results across the five test volumes of different segmentation methods that participated in the (NeoBrainS12, 2012) challenge. The results from the segmentation framework developed in this thesis work correspond to the team labeled as CIMAT_Team in Table V.5. The rest of the reported team names and their corresponding authors are: Picsl_upenn (Wu & Avants, 2012), UCL (Melbourne et al., 2012), ImperialTeam1 (Makropoulos, 2014), DTC (S. Wang, Kuklisova-Murgasova, & Schnabel, 2012) and MCRI (Beare et al., 2016). The team listed as Anonymous1 appears in the (NeoBrainS12, 2012) website <http://neobrainS12.isi.uu.nl> as "under review" and has no associated author as of this date. Three metrics are used for the evaluation: Dice coefficient (DC), mean surface distance (MSD) and Hausdorff distance (HD) (see (İşgum et al., 2015) for the details). The four classes considered for segmentation in this work correspond as follows with the classes reported in the (NeoBrainS12, 2012) website <http://neobrainS12.isi.uu.nl>:

- SGM = basal ganglia and thalami,
- UWM = unmyelinated white matter,
- CGM = cortical gray matter and
- CSF = external cerebrospinal fluid plus ventricles.

Looking at the Dice coefficient (DC) it can be observed in Table V.4 that there is relative consistency between the Dice coefficient values obtained for most of the classes. Specifically, the standard deviation of the Dice coefficient values within each class is: 0.01 for SGM, 0.02 for UWM, 0.05 for CGM and 0.02 for CSF. From those standard deviation values it can be noticed that there is less consistency in the Dice coefficient values obtained for the CGM class relative to the other classes.

Table V.5 shows in yellow the method that performed best in each considered class according to the average Dice coefficient value. The results of the teams are ordered from best to worst in a top row to bottom row fashion according to the average Dice coefficient values for each class group. It can be observed that, according to the average Dice coefficient, the method proposed in this thesis work that corresponds to the label CIMAT_Team achieved competitive results for the four considered classes. The results obtained are: second place for SGM, first place (together with the Anonymous1 team) for UWM, third place for CGM and third place for CSF. (Zijdenbos, Dawant, Margolin, & Palmer, 1994) noted that a Dice coefficient greater than 0.7 can be considered as in excellent agreement with the reference segmentation. Hence, with the exception of the CGM, the results achieved by the segmentation framework proposed in this thesis work could be classified as in excellent agreement with the manual segmentation according to (Zijdenbos et al., 1994). The results for the CGM could be classified as in good agreement with the

manual segmentation. For those reasons, even though the segmentation framework proposed here obtained very competitive results, future work is desired to further improve both the quality and the consistency of the segmentation in the cortical gray matter region.

Class	Testing volume	DC	MSD	HD
SGM	set2_i1	0.878444	0.474384	7.32301
	set2_i2	0.885855	0.417625	4.68976
	set2_i3	0.877868	0.49583	4.22704
	set2_iC1	0.892332	0.317585	3.1212
	set2_iC2	0.900371	0.342816	3.64465
UWM	set2_i1	0.912993	0.328199	6.17781
	set2_i2	0.945126	0.177328	7.49395
	set2_i3	0.904232	0.378075	5.79491
	set2_iC1	0.930497	0.258905	4.77453
	set2_iC2	0.936018	0.235129	4.55462
CGM	set2_i1	0.645045	0.317944	6.6133
	set2_i2	0.764254	0.190288	6.24149
	set2_i3	0.65482	0.339774	6.4225
	set2_iC1	0.671631	0.275186	6.37773
	set2_iC2	0.72657	0.19798	5.46515
CSF	set2_i1	0.811422	0.249234	6.46784
	set2_i2	0.836975	0.168537	6.21114
	set2_i3	0.802712	0.282728	7.2688
	set2_iC1	0.802187	0.246688	6.05227
	set2_iC2	0.857463	0.162599	5.9472

Table V.4: Individual evaluation for each segmented class of the five testing volumes from the 30 weeks corrected age coronal set. The metrics used are the Dice coefficient (DC), the mean surface distance (MSD) and the Hausdorff distance (HD) (Işgum et al., 2015). The evaluation was carried out by the NeoBrainS12 (2012) organizers.

Class	Team	Avg. DC	Avg. MSD	Avg. HD
SGM	Anonymous1	0.90	0.38	5.05
	CIMAT_Team	0.89	0.41	4.60
	UCL*	0.84	0.77	7.99
	ImperialTeam1	0.82	0.76	6.18
	DTC	0.82	0.76	6.77
	MCRI	0.82	0.85	19.78
	Picslupenn*	0.74	1.38	11.26
UWM	CIMAT_Team	0.93	0.28	5.76
	Anonymous1	0.93	0.22	7.28
	ImperialTeam1	0.91	0.30	8.07
	UCL*	0.90	0.34	8.02
	Picslupenn*	0.87	0.46	17.60
	DTC	0.86	0.52	6.03
	MCRI	0.82	0.66	8.36
CGM	Anonymous1	0.75	0.16	5.68
	UCL*	0.71	0.21	6.33
	CIMAT_Team	0.69	0.26	6.22
	ImperialTeam1	0.69	0.25	7.72
	Picslupenn*	0.60	0.48	24.15
	DTC	0.58	0.38	5.66
	MCRI	0.52	0.57	11.26
CSF	Anonymous1	0.86	0.16	6.18
	ImperialTeam1	0.84	0.25	9.69
	CIMAT_Team	0.82	0.22	6.39
	UCL*	0.78	0.27	7.38
	DTC	0.77	0.41	9.21
	MCRI	0.74	0.41	8.69
	Picslupenn*	0.66	0.59	8.15

Table V.5: Average evaluation team results for each segmented class across the five testing volumes from the 30 weeks corrected age coronal set. The metrics used are the Dice coefficient (DC), the mean surface distance (MSD) and the Hausdorff distance (HD) (Iřgum et al., 2015). The team results are ordered descendingly from the top of the table to the bottom of the table according to the average Dice coefficient on each class. The evaluation was carried out by the NeoBrainS12 (2012) organizers. The * indicates that the results have been evaluated over three images (and not five) initially available for the web-based challenge. The data was taken from <http://neobrain12.isi.uu.nl>.

Chapter VI

Conclusions and future work

An automatic and integrated segmentation framework for MRI images of the neonatal brain has been developed in this thesis work. The segmentation framework is an atlas based one and only requires a single individual atlas. Automatic segmentation of neonatal brain MRI images is a very challenging task. Among the top difficulties that this problem presents is the large overlap of the intensity histograms of different neonatal brain tissues, the great variability of the neonatal brain structures, the particularly thin structure of the cortical grey matter and partial volume effects. Chapter III described the overall segmentation framework and the preprocessing steps that it considers, which consist of improving the quality of the MRI input subject and atlas images, extracting the intracranial cavity and aligning the images to the subject space. Then, chapter IV introduced the segmentation stage of the framework, which focuses on enhancing the gray matter tissues at both the cortical and subcortical regions. The segmentation stage uses a Hessian filter, a box filter and post-processing steps to delineate the cortical gray matter and a local neighbourhood with similarity patches in a non-local neighbourhood to improve the segmentation of the subcortical gray matter. Finally, chapter V presented the experiments made to tune the parameters of the segmentation stage of the framework and to identify or discard steps and information at some stages of the framework. The evaluation results of the segmentation framework were also presented in chapter V, which were compared to other methods by means of a recent neonatal brain images segmentation challenge. The proposed segmentation framework obtained state-of-the-art results in the segmentation challenge by ranking among the first three places in every segmented class considered.

VI.1 Future work

Further research is desired for improving the quality of the segmentation at different stages of the framework and for assessing the relevance of different MRI image modalities for neonatal segmentation purposes. For instance it is desired to assess if using only the T1 MRI image modality or only the T2 MRI image modality is enough to obtain the same segmentation results. The evaluation results from chapter V show that the CGM enhancing step needs to be addressed for further improvement. In this regard, other type of filters different from the Hessian filter could be considered, or alternatively the same filter could be considered in such a way that the parameters can be learned in an automatic way. The latter could make it possible to eliminate

the two parameters used at the CGM enhancing step and at the same time improvements in the CGM tissue segmentation could be made by utilizing local information during the parameter learning process. For the preprocessing stage a state-of-the-art super-resolution algorithm could be considered for the isotropic voxel scaling step, possibly yielding that way an improvement in the overall intracranial cavity extraction. Further modifications to the current framework are desirable in order to consider much greater variability inherent in the structures of the non-healthy neonatal brain, for instance in a deformed brain. Lastly the segmentation of other brain tissues could be incorporated into this framework, for instance the cerebellum, the myelinated white matter and the brainstem tissues.

References

- Avants, B., Tustison, N., & Song, G. (2009). Advanced normalization tools (ANTs). In *Insight j*.
- Avants, B. B., Epstein, C. L., Grossman, M., & Gee, J. C. (2008). Symmetric diffeomorphic image registration with cross-correlation: evaluating automated labeling of elderly and neurodegenerative brain. *Medical Image Analysis*, *12*(1), 26–41. Retrieved from <http://www.pubmedcentral.nih.gov/articlerender.fcgi?artid=2276735&tool=pmcentrez&rendertype=abstract> doi: 10.1016/j.media.2007.06.004
- Avants, B. B., Tustison, N. J., Song, G., Cook, P. A., Klein, A., & Gee, J. C. (2011). A reproducible evaluation of ANTs similarity metric performance in brain image registration. *NeuroImage*, *54*(3), 2033–44. Retrieved from <http://www.pubmedcentral.nih.gov/articlerender.fcgi?artid=3065962&tool=pmcentrez&rendertype=abstract> doi: 10.1016/j.neuroimage.2010.09.025
- Beare, R. J., Chen, J., Kelly, C. E., Alexopoulos, D., Smyser, C. D., Rogers, C. E., ... Thompson, D. K. (2016). Neonatal Brain Tissue Classification with Morphological Adaptation and Unified Segmentation. *Frontiers in Neuroinformatics*, *10*(12). doi: <http://doi.org/10.3389/fninf.2016.00012>
- Chudler, E. H. (2015). *Lobes of the Brain*. <https://faculty.washington.edu/chudler/lobe.html>. (Accessed: 2016-06-08)
- Dice, L. R. (1945). Measures of the amount of ecologic association between species. *Ecology*, *26*(3), 297-302.
- Frangi, A. F., Niessen, W. J., Vincken, K. L., & Viergever, M. A. (1998). Multi-scale Vessel Enhancement Filtering. *Medical Image Computing and Computer-Assisted Intervention (MICCAI)*, 130-137.
- Garyfallidis, E., Brett, M., Amirbekian, B., Rokem, A., van der Walt, S., Descoteaux, M., ... Contributors, D. (2014). Dipy, a library for the analysis of diffusion MRI data. *Frontiers in Neuroinformatics*, *8*(8).
- Gui, L., Lisowski, R., Faundez, T., Höppi, P. S., Lazeyras, F., & Kocher, M. (2012). Morphology-driven automatic segmentation of MR images of the neonatal brain. *Medical Image Analysis*, *16*(8), 1565-1579.
- Işgum, I., Benders, M. J. N. L., Avants, B., Cardoso, M. J., Counsell, S. J., Fichi Gomez, E., ... Viergever, M. A. (2015). Evaluation of automatic neonatal brain segmentation algorithms: the NeoBrainS12 challenge. *Medical Image Analysis*, *20*(1), 135-151.
- Liu, C., Frazier, P., & Kumar, L. (2007). Comparative assessment of the measures of thematic classification accuracy. *Remote Sensing of Environment*, *107*(4), 606 - 616. Retrieved from <http://www.sciencedirect.com/science/article/pii/S0034425706004068> doi: <http://dx.doi.org/10.1016/j.rse.2006.10.010>

- Makropoulos, A. (2014). *Automatic MRI segmentation of the developing neonatal brain* (Doctoral thesis). Imperial College London.
- Manjón Herrera, J. V. (2006). *Segmentación Robusta de Imágenes de RM cerebral* (Doctoral thesis). Universidad Politécnica de Valencia.
- Melbourne, A., Cardoso, M. J., Kendall, G. S., Robertson, N. J., Marlow, N., & Ourselin, S. (2012). Neobrain12 challenge: Adaptive neonatal mri brain segmentation with myelinated white matter class and automated extraction of ventricles I-IV. In *MICCAI Grand Challenge on Neonatal Brain Segmentation 2012 (NeoBrainS12)* (p. 16-21).
- NeoBrainS12. (2012). *MICCAI Grand Challenge on Neonatal Brain Segmentation*. Retrieved from <http://neobrain12.isi.uu.nl>
- Ocegueda, O., Dalmau, O., Garyfallidis, E., Descoteaux, M., & Rivera, M. (2016). On the computation of integrals over fixed-size rectangles of arbitrary dimension. *Pattern Recognition Letters*, 79, 68 - 72. Retrieved from <http://www.sciencedirect.com/science/article/pii/S0167865516300861> doi: <http://dx.doi.org/10.1016/j.patrec.2016.05.008>
- Ribas, G. C. (2010). The cerebral sulci and gyri. *Neurosurg Focus*, 28.
- Roselli, M., Matute, E., & Ardila, A. (2010). *Neuropsicología del desarrollo infantil*. El Manual Moderno S.A. de C.V.
- Shi, F., Yap, P.-T., Fan, Y., Cheng, J.-Z., Wald, L. L., Gerig, G., ... Shen, D. (2009). Cortical enhanced tissue segmentation of neonatal brain MR images acquired by a dedicated phased array coil. In *Computer Vision and Pattern Recognition Workshops, 2009. CVPR Workshops 2009. IEEE Computer Society Conference on* (pp. 39-45).
- Tustison, N. J., Avants, B. B., Cook, P. A., Zheng, Y., Egan, A., Yushkevich, P. A., & Gee, J. C. (2010, June). N4ITK: Improved N3 Bias Correction. *IEEE Transactions on Medical Imaging*, 29(6), 1310-1320. doi: 10.1109/TMI.2010.2046908
- Wang, L., Shi, F., Gao, Y., Li, G., Gilmore, J. H., Lin, W., & Shen, D. (2014). Integration of sparse multi-modality representation and anatomical constraint for iso-intense infant brain mr image segmentation. *NeuroImage*, 89, 152-164.
- Wang, S., Kuklisova-Murgasova, M., & Schnabel, J. A. (2012). An atlas-based method for neonatal mr brain tissue segmentation. In *MICCAI Grand Challenge on Neonatal Brain Segmentation 2012 (NeoBrainS12)* (p. 28-35).
- Wu, J., & Avants, B. (2012). Automatic registration-based segmentation for neonatal brains using ANTs and atropos. In *MICCAI Grand Challenge on Neonatal Brain Segmentation 2012 (NeoBrainS12)* (p. 36-47).
- Zijdenbos, A. P., Dawant, B. M., Margolin, R. A., & Palmer, A. C. (1994). Morphometric analysis of white matter lesions in MR images: Method and validation. *IEEE Trans. Med. Imag.*, 13(4), 716-724.